Precision electromagnetic structure of octet baryons in the chiral regime

S. Boinepalli,[1] D. B. Leinweber,[1] A. G. Williams,[1] J. M. Zanotti,[1,2] and J. B. Zhang[1,3]

[1]*Special Research Centre for the Subatomic Structure of Matter and Department of Physics, University of Adelaide 5005, Australia*
[2]*School of Physics, University of Edinburgh, Edinburgh EH9 3JZ, UK*
[3]*Zhejiang Institute of Modern Physics and Department of Physics, Zhejiang University, Hangzhou 310027, People's Republic of China*

The electromagnetic properties of the baryon octet are calculated in quenched QCD on a $20^3 \times 40$ lattice with a lattice spacing of 0.128 fm using the fat-link irrelevant clover (FLIC) fermion action. FLIC fermions enable simulations to be performed efficiently at pion masses as low as 300 MeV. By combining FLIC fermions with an improved-conserved vector current, we ensure that discretization errors occur only at $\mathcal{O}(a^2)$ while maintaining current conservation. Magnetic moments and electric and magnetic radii are extracted from the electric and magnetic form factors for each individual quark sector. From these, the corresponding baryon properties are constructed. Our results are compared with the predictions of quenched chiral perturbation theory. We detect substantial curvature and environment sensitivity of the quark contributions to electric charge radii and magnetic moments in the low quark-mass region.

I. INTRODUCTION

The study of the electromagnetic properties of baryons provides valuable insight into the nonperturbative structure of QCD. Baryon charge radii and magnetic moments provide an excellent opportunity to observe the chiral nonanalytic behavior of QCD. Although the first calculations of hadronic electromagnetic form factors appeared almost 20 years ago [1–3], until recently the state-of-the-art calculations of the electromagnetic properties of octet [4,5] and decuplet [6] baryons and their electromagnetic transitions [7] appeared almost 15 years ago.

However, over the last couple years there has been an increase in activity in the area of octet-baryon electromagnetic structure, mainly by the Adelaide group [8–11] and the QCDSF [12] and LHPC Collaborations [13]. The background field method has also been used recently to explore baryon magnetic moments [14].

In this paper we improve upon our preliminary results reported in Ref. [8] and describe in detail the origin of the lattice simulation results featured in Refs. [9–11] determining the strangeness magnetic moment and charge radius of the nucleon, respectively.

The extraction of baryon masses and electromagnetic form factors proceeds through the calculation of Euclidean two and three-point correlation functions, which are discussed at the hadronic level in Section II B, and at the quark level in Secs. II C and II D. Throughout this analysis we employ the lattice techniques introduced in [4]. We briefly outline the main aspects of these techniques in Sec. III. The correlation functions directly proportional to the electromagnetic form factors of interest are analyzed in Sec. IV. The results are presented and discussed in Sec. V, where an extensive comparison is made with the predictions of quenched chiral perturbation theory ($\mathrm{Q}_\chi\mathrm{PT}$) [15,16]. A summary and discussion of future work is provided in Sec. VI.

II. THEORETICAL FORMALISM

A. Interpolating fields

In this analysis we work with the standard established interpolating fields commonly used in lattice QCD simulations. The notation adopted is similar to that of [4]. To access the proton we use the positive parity interpolating field

$$\chi^{p+}(x) = \epsilon^{abc}(u^{aT}(x)C\gamma_5 d^b(x))u^c(x), \qquad (2.1)$$

where the fields u, d are evaluated at Euclidean space-time point x, C is the charge conjugation matrix, a, b, and c are color labels, and the superscript T denotes the transpose. In this paper we follow the notation of Sakurai. The Dirac γ matrices are Hermitian and satisfy $\{\gamma_\mu, \gamma_\nu\} = 2\delta_{\mu\nu}$, with $\sigma_{\mu\nu} = (1/2i)[\gamma_\mu, \gamma_\nu]$. This interpolating field transforms as a spinor under a parity transformation. That is, if the quark fields $q^a(x)$ ($q = u, d, \cdots$) transform as

$$\mathcal{P}q^a(x)\mathcal{P}^\dagger = +\gamma_0 q^a(\tilde{x}), \qquad (2.2)$$

where $\tilde{x} = (x_0, -\vec{x})$, then

$$\mathcal{P}\chi^{p+}(x)\mathcal{P}^\dagger = +\gamma_0\chi^{p+}(\tilde{x}). \qquad (2.3)$$

The neutron interpolating field is obtained via the exchange $u \leftrightarrow d$, and the strangeness -2, Ξ interpolating fields are obtained by replacing the doubly represented u or d quark fields in Eq. (2.1) by s. Similarly, the charged strangeness -1, Σ interpolating fields are obtained by replacing the singly represented u or d quark fields in Eq. (2.1) by s. For the Σ^0 hyperon one uses [4]

$$\chi^{\Sigma^0}(x) = \frac{1}{\sqrt{2}}\epsilon^{abc}\{(u^{aT}(x)C\gamma_5 s^b(x))d^c(x)$$
$$+ (d^{aT}(x)C\gamma_5 s^b(x))u^c(x)\}, \qquad (2.4)$$

Note that χ^{Σ^0} transforms as a triplet under SU(2) isospin.

An SU(2) isosinglet interpolating field for the Λ can be constructed by replacing " $+$ " $\rightarrow$ " $-$ " in Eq. (2.4). For the SU(3) octet Λ interpolating field, one has

$$
\begin{aligned}
\chi^{\Lambda}(x) = \frac{1}{\sqrt{6}} \epsilon^{abc} \{ & 2(u^{aT}(x) C \gamma_5 d^b(x)) s^c(x) \\
& + (u^{aT}(x) C \gamma_5 s^b(x)) d^c(x) \\
& - (d^{aT}(x) C \gamma_5 s^b(x)) u^c(x) \}.
\end{aligned}
\tag{2.5}
$$

We select this interpolating field for studying the Λ in the following.

B. Correlation functions at the hadronic level

The extraction of baryon masses and electromagnetic form factors proceeds through the calculation of the ensemble average (denoted $\langle \cdots \rangle$) of two and three-point correlation functions. The two-point function is defined as

$$
\langle G^{BB}(t; \vec{p}, \Gamma) \rangle = \sum_{\vec{x}} e^{-i\vec{p} \cdot \vec{x}} \Gamma^{\beta\alpha} \langle \Omega | T(\chi^{\alpha}(x) \bar{\chi}^{\beta}(0)) | \Omega \rangle.
\tag{2.6}
$$

Here Ω represents the QCD vacuum, Γ is a 4×4 matrix in Dirac space and α, β are Dirac indices. At the hadronic level we insert a complete set of states $|B, p, s\rangle$ and define

$$
\langle \Omega | \chi(0) | B, p, s \rangle = Z_B(p) \sqrt{\frac{M}{E_p}} u(p, s),
\tag{2.7}
$$

where $Z_B(p)$ represents the coupling strength of $\chi(0)$ to baryon B, and $E_p = \sqrt{\vec{p}^2 + M^2}$. A momentum dependence for $Z_B(p)$ is included for the case where a smeared sink is employed. For large Euclidean time

$$
\langle G^{BB}(t; \vec{p}, \Gamma) \rangle \simeq \frac{Z_B(p) \bar{Z}_B(p)}{2E_p} e^{-E_p t} \text{tr}[\Gamma(-i\gamma \cdot p + M)].
\tag{2.8}
$$

Here $\bar{Z}_B(p)$ is the coupling strength of the source $\bar{\chi}(0)$ to the baryon. Again, the momentum dependence allows for the use of smeared fermion sources in the creation of the quark propagators and the differentiation between source and sink allows for our use of smeared sources and point sinks in the following. Similarly the three-point correlation function for the electromagnetic current, $j^{\mu}(x)$, is defined as

$$
\begin{aligned}
\langle G^{Bj^{\mu}B}(t_2, t_1; \vec{p}', \vec{p}; \Gamma) \rangle = \sum_{\vec{x}_2, \vec{x}_1} & e^{-i\vec{p}' \cdot \vec{x}_2} e^{+i(\vec{p}' - \vec{p}) \cdot \vec{x}_1} \Gamma^{\beta\alpha} \\
& \times \langle \Omega | T(\chi^{\alpha}(x_2) j^{\mu}(x_1) \bar{\chi}^{\beta}(0)) | \Omega \rangle.
\end{aligned}
\tag{2.9}
$$

For large Euclidean time separations $t_2 - t_1 \gg 1$ and $t_1 \gg 1$, the three-point function at the hadronic level is dominated by the contribution from the ground state

$$
\begin{aligned}
\langle G^{Bj^{\mu}B}(t_2, t_1; \vec{p}', \vec{p}; \Gamma) \rangle = \sum_{s, s'} & e^{-E_{p'}(t_2 - t_1)} e^{-E_p t_1} \Gamma^{\beta\alpha} \\
& \times \langle \Omega | \chi^{\alpha} | p', s' \rangle \langle p', s' | j^{\mu} | p, s \rangle \\
& \times \langle p, s | \bar{\chi}^{\beta} | \Omega \rangle.
\end{aligned}
\tag{2.10}
$$

The matrix element of the electromagnetic current has the general form

$$
\begin{aligned}
\langle p', s' | j^{\mu} | p, s \rangle = \left(\frac{M^2}{E_p E_{p'}} \right)^{1/2} & \bar{u}(p', s') \\
& \times \left(F_1(q^2) \gamma^{\mu} - F_2(q^2) \sigma^{\mu\nu} \frac{q^{\nu}}{2M} \right) u(p, s),
\end{aligned}
\tag{2.11}
$$

where $q = p' - p$. To eliminate the time dependence of the three-point functions we construct the following ratio,

$$
R(t_2, t_1; \vec{p}', \vec{p}; \Gamma, \Gamma'; \mu) = \left[\frac{\langle G^{Bj^{\mu}B}(t_2, t_1; \vec{p}', \vec{p}; \Gamma) \rangle \langle G^{Bj^{\mu}B}(t_2, t_1; -\vec{p}, -\vec{p}'; \Gamma) \rangle}{\langle G^{BB}(t_2; \vec{p}'; \Gamma') \rangle \langle G^{BB}(t_2; -\vec{p}; \Gamma') \rangle} \right]^{1/2}.
\tag{2.12}
$$

For large time separations $t_2 - t_1 \gg 1$ and $t_1 \gg 1$ this ratio is constant in time and is proportional to the electromagnetic form factors of interest. We further define a reduced ratio $\bar{R}(\vec{p}', \vec{p}; \Gamma, \Gamma'; \mu)$ as

$$
\bar{R}(\vec{p}', \vec{p}; \Gamma, \Gamma'; \mu) = \left[\frac{2E_p}{E_p + M} \right]^{1/2} \left[\frac{2E_{p'}}{E_{p'} + M} \right]^{1/2} R(t_2, t_1; \vec{p}', \vec{p}; \Gamma, \Gamma'; \mu),
\tag{2.13}
$$

from which the Sachs forms for the electromagnetic form factors

$$
\mathcal{G}_E(q^2) = F_1(q^2) - \frac{q^2}{(2M)^2} F_2(q^2),
\tag{2.14}
$$

$$
\mathcal{G}_M(q^2) = F_1(q^2) + F_2(q^2),
\tag{2.15}
$$

may be extracted through an appropriate choice of Γ and Γ'. A straight forward calculation reveals

$$
\mathcal{G}_E(q^2) = \bar{R}(\vec{q}, \vec{0}; \Gamma_4, \Gamma_4, 4),
\tag{2.16}
$$

$$
|\epsilon_{ijk} q^i| \mathcal{G}_M(q^2) = (E_q + M) \bar{R}(\vec{q}, \vec{0}; \Gamma_j, \Gamma_4, k),
\tag{2.17}
$$

$$
|q^k| \mathcal{G}_E(q^2) = (E_q + M) \bar{R}(\vec{q}, \vec{0}; \Gamma_4, \Gamma_4, k),
\tag{2.18}
$$

where

$$\Gamma_j = \frac{1}{2}\begin{pmatrix} \sigma_j & 0 \\ 0 & 0 \end{pmatrix}, \qquad \Gamma_4 = \frac{1}{2}\begin{pmatrix} I & 0 \\ 0 & 0 \end{pmatrix}. \qquad (2.19)$$

C. Correlation functions at the quark level

Here the two and three-point functions of Sec. II B are calculated at the quark level by using the explicit forms of the interpolating fields of Sec. II A and contracting out all possible pairs of quark-field operators. These become quark propagators in the ensemble average. For convenience, we introduce the shorthand notation for the correlation functions $\mathcal{G}$ of quark propagators S

$$\mathcal{G}(S_{f_1}, S_{f_2}, S_{f_3}) \equiv \epsilon^{abc}\epsilon^{a'b'c'}\{S_{f_1}^{aa'}(x, 0) \\
\times \text{tr}[S_{f_2}^{bb'T}(x, 0)S_{f_3}^{cc'}(x, 0)] \\
+ S_{f_1}^{aa'}(x, 0)S_{f_2}^{bb'T}(x, 0)S_{f_3}^{cc'}(x, 0)\}, \quad (2.20)$$

where $S_{f_{1-3}}^{aa'}(x, 0)$ are the quark propagators in the background link-field configuration U corresponding to flavors f_{1-3}. This allows us to express the correlation functions in a compact form. The associated correlation function for χ^{p+} can be written as

$$G^{p+}(t, \vec{p}; \Gamma) = \left\langle \sum_{\vec{x}} e^{-i\vec{p}\cdot\vec{x}} \text{tr}[\Gamma\mathcal{G}(S_u, \tilde{C}S_d\tilde{C}^{-1}, S_u)] \right\rangle,$$

$$(2.21)$$

FIG. 1. Diagrams illustrating the two topologically different insertions of the current within the framework of lattice QCD.

where $\langle \cdots \rangle$ is the ensemble average over the link fields, Γ is the $\Gamma_\pm$ projection operator that separates the positive and negative parity states, and $\tilde{C} = C\gamma_5$. For ease of notation, we will drop the angled brackets, $\langle \cdots \rangle$, and all the following correlation functions will be understood to be ensemble averages.

Two-point correlation functions for other octet baryons composed of a doubly-represented quark flavor and a singly-represented quark flavor follow from Eq. (2.21) with the appropriate substitution of flavor subscripts. The correlation function for the neutral member Σ^0 is given by the average of correlation functions for the charged states Σ^+ and Σ^-. Finally the correlation function for Λ obtained from the octet-interpolating field of Eq. (2.5) is

$$G^{\Lambda^8}(t, \vec{p}; \Gamma) = \frac{1}{6}\sum_{\vec{x}} e^{-i\vec{p}\cdot\vec{x}} \text{tr}[\Gamma\{2\mathcal{G}(S_s, \tilde{C}S_u\tilde{C}^{-1}, S_d) + 2\mathcal{G}(S_s, \tilde{C}S_d\tilde{C}^{-1}, S_u) + 2\mathcal{G}(S_d, \tilde{C}S_u\tilde{C}^{-1}, S_s) + 2\mathcal{G}(S_u, \tilde{C}S_d\tilde{C}^{-1}, S_s)$$

$$- \mathcal{G}(S_d, \tilde{C}S_s\tilde{C}^{-1}, S_u) - \mathcal{G}(S_u, \tilde{C}S_s\tilde{C}^{-1}, S_d)\}]. \qquad (2.22)$$

D. Three-point functions at the quark level

In determining the three-point function, one encounters two topologically different ways of performing the current insertion. Figure 1 displays skeleton diagrams for these two insertions. These diagrams may be dressed with an arbitrary number of gluons (and additional sea-quark loops in full QCD). Diagram (a) illustrates the connected insertion of the current to one of the quarks created via the baryon interpolating field. This simple skeleton diagram does indeed contain a sea-quark component, as upon dressing the diagram with gluon exchange, quark-loop and
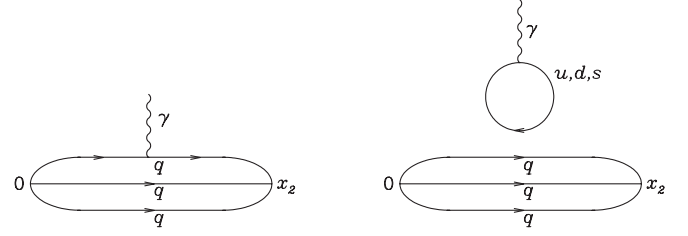
Z-diagrams flows become possible. It is here that "Pauli-blocking" in the sea contributions, central to obtaining violation of the Gottfried sum rule, are taken into account. Diagram (b) accounts for an alternative quark-field contraction where the current first produces a disconnected $q\bar{q}$ loop-pair which in turn interacts with the valence quarks of the baryon via gluons.

Thus, the number of terms in the three-point function is 4 times that in Eq. (2.21). The correlation function for proton matrix elements obtained from the interpolator of Eq. (2.1) is

$$T(\chi^{p+}(x_2)j^\mu(x_1)\bar{\chi}^{p+}(0)) = \mathcal{G}(\hat{S}_u(x_2, x_1, 0), \tilde{C}S_d(x_2, 0)\tilde{C}^{-1}, S_u(x_2, 0)) + \mathcal{G}(S_u(x_2, 0), \tilde{C}S_d(x_2, 0)\tilde{C}^{-1}, \hat{S}_u(x_2, x_1, 0))$$

$$+ \mathcal{G}(S_u(x_2, 0), \tilde{C}\hat{S}_d(x_2, x_1, 0)\tilde{C}^{-1}, S_u(x_2, 0))$$

$$+ \sum_{q=u,d,s} e_q \sum_i \text{tr}[S_q^{ii}(x_1, x_1)\gamma_\mu]\mathcal{G}(S_u(x_2, 0), \tilde{C}S_d(x_2, 0)\tilde{C}^{-1}, S_u(x_2, 0)), \qquad (2.23)$$

where

$$\hat{S}_q^{aa'}(x_2, x_1, 0) = e_q \sum_i S_q^{ai}(x_2, x_1) \gamma_\mu S_q^{ia'}(x_1, 0), \quad (2.24)$$

denotes the connected insertion of the electromagnetic current to a quark of charge e_q.

The first two terms of Eq. (2.23) provide the connected insertion contribution of the u-quark sector to the proton's electromagnetic properties, whereas the third term provides the connected d-quark contribution. The latter term of Eq. (2.23) accounts for the "disconnected" loop contribution depicted in Fig. 1(b). Here, the sum over the quarks running around the loop has been restricted to the flavors relevant to the ground state baryon octet. In the SU(3)-flavor limit the sum vanishes for the electromagnetic current. However, the heavier strange-quark mass allows for a nontrivial result.

The disconnected current insertion requires a numerical estimate of $S_q^{ii}(x_1, x_1)$ for the lattice volume of diagonal spatial indices. As this requires numerous source vectors in the fermion-matrix inversion, determination of this propagator is numerically intensive [17–19]. Indeed, an indirect method using experimental results, chiral effective field theory and the lattice results from the connected current insertion presented herein, provides the most precise determinations of these quark-loop contributions to the nucleon's electromagnetic structure [9–11] at present. This approach should be viewed as complementary to an *ab initio* determination via lattice QCD which awaits a next-generation dynamical-fermion simulation of QCD [15].

It is interesting to examine the structure of the connected insertion contributions to the proton's structure. Here, we see very different roles played by u and d quarks in the correlation function, in that only the d quark appears in the second position of $\mathcal{G}$. The absence of equivalence for u and d contributions allows the connected quark sector to give rise to a nontrivial neutron charge radius, a large neutron magnetic moment, or a violation of the Gottfried sum rule. As each term of Eq. (2.23) can be calculated individually, it is a simple task to isolate the quark-sector contributions to the baryon electromagnetic properties.

Another interesting point to emphasize, is that there is no simple relationship between the properties of a particular quark flavor bound in different baryons. For example, the correlator for Σ^+ is given by (2.23) with $d \to s$. Hence, a u-quark propagator in Σ^+ is multiplied by an s-quark propagator, whereas in the proton the u-quark propagators are multiplied by a d-quark propagator. The different mass of the neighboring quark gives rise to an environment sensitivity in the u-quark contributions to observables [4,6,7,9,20–22]. This point sharply contrasts the concept of an intrinsic quark property which is independent of the quark's environment. This concept of an intrinsic quark property is a fundamental foundation of many constituent based quark models and is not in accord with QCD.

III. LATTICE TECHNIQUES

A. Gauge and quark actions

The simulations are performed using the mean-field $\mathcal{O}(a^2)$-improved Luscher-Weisz [23] plaquette plus rectangle gauge action on a $20^3 \times 40$ lattice with periodic boundary conditions. The lattice spacing $a = 0.128$ fm is determined by the Sommer scale $r_0 = 0.50$ fm [24]. This large-volume lattice ensures a good density of low-lying momenta which are key to giving rise to chiral nonanalytic behavior in the observables simulated on the lattice [9–11].

We perform a high-statistics analysis using a large sample of 400 configurations for our lightest eight quark masses. We also consider a subset of 200 configurations for our three heaviest quark masses to explore the approach to the heavy-quark regime. A subensemble bias correction is applied multiplicatively to the heavy-quark results, by matching the central values of the 200 configuration subensemble and 400 configuration ensemble averages at $\kappa = 0.12780$. The error analysis is performed by a third-order, single-elimination jackknife.

For the quark fields, we use the fat-link irrelevant clover fermion action [25]

$$S_{\text{SW}}^{\text{FL}} = S_{\text{W}}^{\text{FL}} - \frac{ig C_{\text{SW}} \kappa r}{2(u_0^{\text{FL}})^4} \bar{\psi}(x) \sigma_{\mu\nu} F_{\mu\nu} \psi(x), \quad (3.1)$$

where $F_{\mu\nu}$ is an $\mathcal{O}(a^4)$-improved lattice definition [26] constructed using fat links and u_0^{FL} is the plaquette measure of the mean link calculated with fat links. The mean-field improved fat-link irrelevant Wilson action is

$$S_{\text{W}}^{\text{FL}} = \sum_x \bar{\psi}(x) \psi(x) + \kappa \sum_{x,\mu} \bar{\psi}(x) \left[\gamma_\mu \left(\frac{U_\mu(x)}{u_0} \psi(x + \hat{\mu}) \right. \right.$$
$$\left. - \frac{U_\mu^\dagger(x - \hat{\mu})}{u_0} \psi(x - \hat{\mu}) \right)$$
$$\left. - r \left(\frac{U_\mu^{\text{FL}}(x)}{u_0^{\text{FL}}} \psi(x + \hat{\mu}) + \frac{U_\mu^{\text{FL}\dagger}(x - \hat{\mu})}{u_0^{\text{FL}}} \psi(x - \hat{\mu}) \right) \right],$$
$$(3.2)$$

with $\kappa = 1/(2m + 8r)$. We take the standard value $r = 1$. Our notation uses the Pauli representation of the Dirac γ-matrices [27], where the γ-matrices are hermitian and $\sigma_{\mu\nu} = [\gamma_\mu, \gamma_\nu]/(2i)$. Fat links are constructed by performing $n_{\text{APE}} = 6$ sweeps of APE smearing, where in each sweep the weights given to the original link and the six transverse staples are 0.3 and $(0.7/6)$, respectively. The FLIC action is closely related to the mean-field improved clover (MFIC) fermion action in that the latter is described by Eqs. (3.1) and (3.2) with all fat-links replaced by untouched thin links and $F_{\mu\nu}$ defined by the 1×1-loop clover definition.

TABLE I. Hadron masses in appropriate powers of GeV for various values of the hopping parameter, κ. For reference, experimentally measured values are indicated at the end of the table.

κ	m_π^2	N	Λ	Σ	Ξ
0.12630	0.9972(55)	1.829(8)	1.728(10)	1.700(9)	1.612(11)
0.12680	0.8947(54)	1.763(9)	1.681(10)	1.656(10)	1.586(12)
0.12730	0.7931(53)	1.695(9)	1.632(11)	1.566(11)	1.558(12)
0.12780	0.6910(35)	1.629(10)	1.584(10)	1.570(10)	1.531(10)
0.12830	0.5925(33)	1.554(10)	1.530(10)	1.521(10)	1.502(10)
0.12885	0.4854(31)	1.468(11)	1.468(11)	1.468(11)	1.468(11)
0.12940	0.3795(31)	1.383(11)	1.406(11)	1.417(11)	1.435(11)
0.12990	0.2839(33)	1.301(11)	1.347(11)	1.371(11)	1.404(11)
0.13025	0.2153(35)	1.243(12)	1.303(12)	1.341(12)	1.382(11)
0.13060	0.1384(43)	1.190(15)	1.256(13)	1.313(12)	1.359(11)
0.13080	0.0939(44)	1.159(21)	1.226(16)	1.296(14)	1.346(11)
experiment	0.0196	0.939	1.116	1.189	1.315

For fat links, the mean link $u_0 \approx 1$, indicating that perturbative renormalizations are small for smeared links and are accurately accounted for by small mean-field improvement corrections. As a result, mean-field improvement of the coefficients of the clover and Wilson terms of the fermion action is sufficient to accurately match these terms and eliminate $\mathcal{O}(a)$ errors from the fermion action [28]. An added advantage is that access to the light-quark mass regime is enabled by the improved chiral properties of the FLIC fermion action [29].

Time slices are labeled from 1 to 40, and a fixed boundary condition at $t = 40$ is used for the fermions. An analysis of the pion correlator indicates that the effects of this boundary condition are negligible for $t \leq 30$, and all of our correlation-function fits are performed well within this regime.

Gauge-invariant Gaussian smearing [30,31] in the spatial dimensions is applied at the source at $t = 8$ to increase the overlap of the interpolating operators with the ground state while suppressing excited-state contributions.

Table I provides the kappa values used in our simulations, together with the calculated π and octet-baryon masses. While we refer to m_π^2 to infer the quark masses, we note that the critical value where the pion mass vanishes is $\kappa_{\mathrm{cr}} = 0.13135$.

We select $\kappa = 0.12885$ to represent the strange quark in this simulation. At this κ the $s\bar{s}$ pseudoscalar mass is 0.697 GeV, which compares well with the experimental value of $2m_K^2 - m_\pi^2 = (0.693 \text{ GeV})^2$, motivated by leading order chiral perturbation theory.

B. Improved-conserved vector current

For the construction of the $\mathcal{O}(a)$-improved-conserved vector current, we follow the technique proposed by Martinelli *et al.* [32]. The standard conserved vector current for Wilson-type fermions is derived via the Noether procedure

$$j_\mu^{\mathrm{C}} \equiv \tfrac{1}{4}[\bar{\psi}(x)(\gamma_\mu - r)U_\mu(x)\psi(x + \hat{\mu}) \\ + \bar{\psi}(x + \hat{\mu})(\gamma_\mu + r)U_\mu^\dagger(x)\psi(x) + (x \to x - \hat{\mu})].$$

(3.3)

The $\mathcal{O}(a)$-improvement term is also derived from the fermion action and is constructed in the form of a total four-divergence, preserving charge conservation. The $\mathcal{O}(a)$-improved-conserved vector current is

$$j_\mu^{\mathrm{CI}} \equiv j_\mu^{\mathrm{C}}(x) + \frac{r}{2}C_{CVC}a\sum_\rho \partial_\rho(\bar{\psi}(x)\sigma_{\rho\mu}\psi(x)), \quad (3.4)$$

where C_{CVC} is the improvement coefficient for the conserved vector current and we define

$$\partial_\rho(\bar{\psi}(x)\psi(x)) \equiv \bar{\psi}(x)(\overleftarrow{\nabla}_\rho + \overrightarrow{\nabla}_\rho)\psi(x), \quad (3.5)$$

where the forward and backward derivatives are defined as

$$\overrightarrow{\nabla}_\mu\psi(x) = \frac{1}{2a}[U_\mu(x)\psi(x + \hat{\mu}) - U_\mu^\dagger(x - \hat{\mu})\psi(x - \hat{\mu})],$$
$$\bar{\psi}(x)\overleftarrow{\nabla}_\mu = \frac{1}{2a}[\bar{\psi}(x + \hat{\mu})U_\mu^\dagger(x) - \bar{\psi}(x - \hat{\mu})U_\mu(x - \hat{\mu})].$$

The terms proportional to the Wilson parameter r in Eq. (3.3) and the four-divergence in Eq. (3.4) have their origin in the irrelevant operators of the fermion action and vanish in the continuum limit. Nonperturbative improvement is achieved by constructing these terms with fat-links. As we have stated, perturbative corrections are small for fat-links and the use of the tree-level value for $C_{CVC} = 1$ together with small mean-field improvement corrections ensures that $\mathcal{O}(a)$ artifacts are accurately removed from the vector current. This is only possible when the current is constructed with fat links. Otherwise, C_{CVC} needs to be appropriately tuned to ensure all $\mathcal{O}(a)$ artifacts are removed.

In order to suppress contributions from excited states, large Euclidean times are required, both following the source at t_0, and following the current insertion at t_1. Our two-point function analysis indicates that the ground state is isolated well by $t = 14$, largely due to an excellent selection for the source smearing parameters. Therefore the current insertion is performed at $t_1 = 14$.

We note that the precision of our results is sufficient to reveal a small excited-state contamination in the correlation function at the position of the current insertion. There is always a systematic error associated with excited-state contaminations and ideally this error is simply hidden in the statistical uncertainties.

A comparison of the asymptotic masses with those obtained from a fit including the onset of the point-split current reveals a 2% admixture of excited-state contamination in our lightest five quark masses and smaller for heavier quark masses. This error is typically small relative to the statistical errors of the quantities of interest and do not affect the interpretation of our results.

C. Improved unbiased estimators

The two and three-point correlation functions are defined as averages over an infinite ensemble of equilibrium gauge field configurations, but are approximated by an average over a finite number of configurations. To minimize the noise in the results, we exploit the parity of the correlation functions [33]

$$G(\vec{p}', \vec{p}, \vec{q}; \Gamma) = s_P G(-\vec{p}', -\vec{p}, -\vec{q}; \Gamma), \qquad s_P = \pm 1, \tag{3.6}$$

and calculate them for both $\vec{p}$, $\vec{p}'$, $\vec{q}$, and $-\vec{p}$, $-\vec{p}'$, $-\vec{q}$. While this requires an extra matrix inversion to determine $\hat{S}(x_2, 0; t_1, -\vec{q}, \mu)$, the ratio of three- to two-point functions is determined with a substantial reduction in the statistical uncertainties. The improvement is better than that obtained by doubling the number of configurations.

Similarly, the link variables $\{U\}$ and $\{U^*\}$ are gauge field configurations of equal weight, and therefore we account for both sets of configurations in calculating the correlation functions [34]. With the fermion-matrix property

$$M(\{U^*\}) = (\tilde{C}M(\{U\})\tilde{C}^{-1})^*, \tag{3.7}$$

it follows that

$$S(x, 0; \{U^*\}) = (\tilde{C}S(x, 0; \{U\})\tilde{C}^{-1})^*, \tag{3.8}$$

$$\hat{S}(x, 0; t, \vec{q}, \mu; \{U^*\}) = (\tilde{C}\,\hat{S}(x, 0; t, -\vec{q}, \mu; \{U\})\tilde{C}^{-1})^*, \tag{3.9}$$

and therefore the correlation functions are purely real provided

$$\Gamma = s_C(\tilde{C}\Gamma\tilde{C}^{-1})^* \quad \text{and} \quad s_C = s_P. \tag{3.10}$$

These conditions are satisfied with the selections for

Γ indicated in Eq. (2.19). In summary, the inclusion of both $\{U\}$ and $\{U^*\}$ configurations in the calculation of the correlation functions provides an improved unbiased estimate of the ensemble average properties incorporating parity symmetry and significantly reducing statistical fluctuations.

D. Fit regime selection criteria

In fitting the correlation functions, the covariance-matrix based χ^2 per degree of freedom (d.o.f.) plays a central role.

The correlated χ^2/dof is given by

$$\frac{\chi^2}{\text{dof}} = \frac{1}{N_t - M} \sum_{i=1}^{N_t} \sum_{j=1}^{N_t} (y(t_i) - T(t_i)) C^{-1}(t_i, t_j)(y(t_j) - T(t_j)), \tag{3.11}$$

where, M is the number of parameters to be fitted, N_t is the number of time slices considered, $y(t_i)$ is the configuration average value of the dependent variable at time t_i that is being fitted to a theoretical value $T(t_i)$, and $C(t_i, t_j)$ is the covariance matrix. The elements of the covariance matrix are estimated via the jackknife method

$$C(t_i, t_j) = \frac{N_c - 1}{N_c} \sum_{m=1}^{N_c} [\bar{y}_m(t_i) - \bar{\bar{y}}(t_i)][\bar{y}_m(t_j) - \bar{\bar{y}}(t_j)], \tag{3.12}$$

$$= (N_c - 1) \times \left\{ \frac{1}{N_c} \sum_{m=1}^{N_c} \bar{y}_m(t_i)\bar{y}_m(t_j) - \bar{\bar{y}}(t_i)\bar{\bar{y}}(t_j) \right\}, \tag{3.13}$$

where N_c is the total number of configurations and $\bar{y}_m(t_i)$ is the jackknife ensemble average of the system after removing the mth configuration. $\bar{\bar{y}}(t_i)$ is the average of all such jackknife averages, given by

$$\bar{\bar{y}}(t_i) = \frac{1}{N_c} \sum_{m=1}^{N_c} \bar{y}_m(t_i). \tag{3.14}$$

In the process of selecting the fit regimes, numerous fits are performed over a variety of start times and a variety of time durations. The following criteria are taken into account in selecting the preferred fit regime:

(1) The $\chi^2/\text{d.o.f.}$ is monitored and plays a significant role in determining the start time of the fit. Values within the range 0.5 to 1.5 are preferred and it is often possible to select a regime providing a perfect fit measure of 1. Start times for which the $\chi^2/\text{d.o.f.}$ increases significantly as the duration of the regime is increased are discarded. In practice, the $\chi^2/\text{d.o.f.}$ sets a lower bound for the start time, and other criteria may lead to a later start time for the fit.

(2) In some cases a monotonic systematic drift can be observed in the ratio of correlation functions (2.12) which otherwise should be constant in time.

Often the drift is sufficiently small to provide a $\chi^2/\text{d.o.f.} < 1.5$. In these few cases, a later start time is selected to ensure that sufficient Euclidean time evolution has occurred to accurately isolate the ground state, suppressing systematic errors at the expense of larger statistical errors.

(3) As the quarks become lighter, the spacing between the ground and first excited states of the baryon spectrum becomes larger [34,35], due to the more rapid reduction in the mass of the lower-lying state. This provides improved exponential suppression of excited-state contaminations. Hence, as one approaches the light-quark mass regime, a monotonic reduction in the starting time-slice of the fit regime may be possible.

(4) As the quark masses become lighter, the signal is lost to noise at earlier times. Hence the final time slice of the fit window is also monotonically decreased as the quarks become lighter. We typically consider fit regimes of three to five time slices and preferably the latter when the signal is not obviously lost to noise.

For quark masses lighter than the strange-quark mass, the splittings between adjacent quark masses are calculated and fit using the same techniques. By considering adjacent splittings, excited-state contributions, which are less dependent on the quark mass (see item 3 above), are suppressed in taking the difference before fitting. The physics behind this is well motivated as more of the excited state's energy comes from sources other than the quark masses. For example, it is well established that the slope of excited-state masses with respect to m_π^2, is smaller than the ground state slope for $m_\pi^2 > 0.1 \text{ GeV}^2$.

In practice, we find that excited-state contaminations are reduced by fitting the difference. To illustrate this we first establish a common time-slice fit window for a direct fit of the two correlation functions. Upon applying the same fit regime to a fit of their difference, we find the $\chi^2/\text{d.o.f.}$ to be small. This is an indication of the removal of excited-state contamination in the difference of the correlation functions.

In determining the optimal fit regime, the covariance-matrix based $\chi^2/\text{d.o.f.}$ is used to guide the selection of the fit window. In practice, good $\chi^2/\text{d.o.f.}$ are found one to two time slices earlier.

A precise examination of the environment sensitivity of quark-sector contributions to baryon electromagnetic properties lies at the core of this investigation. For example, the doubly-represented u quark in the proton is to be compared with the doubly-represented u quark in Σ^+; the singly-represented u quark in the neutron with the u quark in Ξ^0. Similarly, it is interesting to compare the strange and light-quark sectors of Ξ^- with those of Λ. Conventional models reverse the ordering of the observed magnetic moments. After the consideration of the preceding criteria, the fit

regimes are unified for each of the quark-sector contributions wherever possible. This comparison is done for each value of κ governing the quark mass, reducing systematic errors associated with choosing different time-fitting regimes for similar quantities. For example, for the case of the doubly-represented u quark in the proton and Σ^+, it is possible to equate the fit regimes for all but the two lightest quark masses where the $\chi^2/\text{d.o.f.}$ insists on different fit regimes.

IV. CORRELATION-FUNCTION ANALYSIS

The following calculations are performed with $\vec{p} = 0$, $\vec{p}' = \vec{q} = |\vec{q}|\hat{x}$ at $q_x a = 2\pi/L_x$ with $L_x = 20$, the minimum nonzero momentum available on our lattice. We introduce $Q^2 = -q^2$, as q^2 is negative (spacelike). While Q^2 is dependent on the mass of the baryon, we find this mass dependence to be small. Indeed all form factors may be regarded as being calculated at $Q^2 = 0.227 \pm 0.002 \text{ GeV}^2$, where the error is dominated by the mass dependence of the target baryon. Where a spatial direction of the electromagnetic current is required, it is chosen to be the z-direction. Electric and magnetic form factors are extracted from our correlation functions as described in Eqs. (2.16) and (2.17).

A. Baryon masses

The masses of the baryon octet are plotted against m_π^2 in Fig. 2 and are tabulated in Table I. We observe the $SU(3)_f$ limit at our sixth quark mass. The mass splitting between Σ and Λ at the lowest pion mass ($m_\pi = 0.3064 \pm 0.0072 \text{ GeV}$) on our lattice is $69 \pm 2 \text{ MeV}$ which is only slightly smaller than the experimentally measured splitting of 76 MeV. Hence the generic features of the baryon-octet mass spectrum is reproduced well in our quenched simulation.
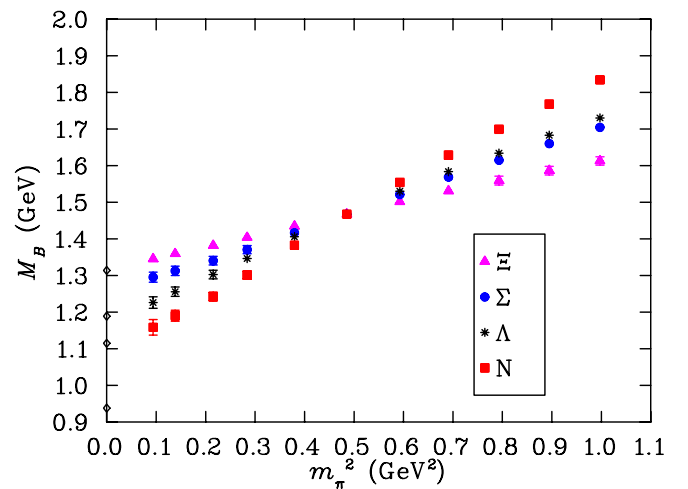

FIG. 2 (color online). Masses of the octet baryons. The SU(3) flavor limit is evident. Points on the y-axis indicate the experimentally measured masses for reference.

B. Form factor correlators

In general, the baryon form factors are calculated on a quark-sector by quark-sector basis with each sector normalized to the contribution of a single quark with unit charge. Hence to calculate the corresponding baryon property, each quark-sector contribution should be multiplied by the appropriate charge and quark number. Under such a scheme for a generic form factor f, the proton form factor, f_p, is obtained from the u- and d-quark sectors normalized for a single quark of unit charge via

$$f_p = 2 \times \tfrac{2}{3} \times f_u + 1 \times (-\tfrac{1}{3}) \times f_d. \qquad (4.1)$$

The electric form factor of the proton and contributions from the u- and d-quark sectors are plotted in Fig. 3 as a function of Euclidean time at the SU(3)-flavor limit. Here, charge and quark number factors have been included such that the proton result is simply the sum of the illustrated quark sectors. The lines indicate the time slices selected for the fit using the considerations of Sec. III D.

We find that substantial Euclidean time evolution is required following the current insertion to obtain acceptable values of the $\chi^2/\text{d.o.f.}$; in this case seven time slices following the current insertion at $t_1 = 14$.

For light-quark masses lighter than the strange-quark mass, we fit the change in the form factor ratios of Eqs. (2.16) or (2.17) from one quark mass to the next and add this to the previous result at the heavier quark mass. Figure 4 shows the quark-sector contributions (including charge and quark number factors) to the electric form factor of the proton at $Q^2 = 0.227(2)$ (GeV^2) as a function of Euclidean time, t_2, for the ninth quark mass where $m_\pi^2 = 0.2153(35)$ GeV^2. The correlator is obtained from the splitting between the ninth and eighth quark-mass states and this difference is added to the result previously estab-
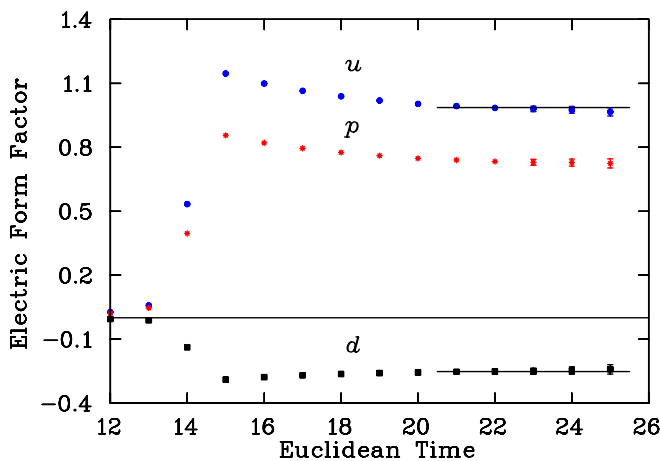
lished for the eighth quark mass. The improvement of the plateau is apparent in Fig. 4. It is clear that one could go all the way to the current insertion at time slice 14 and make only a small systematic error. However, the statistical precision of our results does not allow us to do so. In most cases, substantial Euclidean time evolution is required to obtain an acceptable $\chi^2/\text{d.o.f.}$

Tables II, III, IV, and V list the electric form factors for all the octet baryons at the quark level for the 11 quark masses considered. In the tables, the selected time frame, the fit value and the associated $\chi^2/\text{d.o.f.}$ are indicated.

Turning now to the magnetic form factors, Fig. 5 shows the magnetic form factor of Ξ^0 and its quark sectors (including charge and quark number factors) as a function of Euclidean time at the SU(3)-flavor limit. Preferred fit windows following from the criteria of Sec. III D and best fit values are indicated.

Here the conversion from the natural magneton, $e/(2m_B)$, where the mass of the baryon under investigation appears, to the nuclear magneton, $e/(2m_N)$, where the physical nucleon mass appears, has been done by multiplying the lattice form factor results by the ratio m_N/m_B. In this way the form factors are presented in terms of a constant unit; i.e. the nuclear magneton.

The negative contribution of the u quark to the total form factor indicates that its spin is on average opposite to that of the doubly represented s quarks. This, as well the relative magnitude of the contributions, is in qualitative agreement with simple constituent quark models based on SU(6) spin-flavor symmetry.

In Fig. 6 we present the Euclidean time dependence of the magnetic form factors of Ξ^0 calculated at the ninth

FIG. 3 (color online).   Electric form factor of the proton and its quark sectors (including charge and quark number factors) at $Q^2 = 0.227(2)$ GeV^2 as a function of Euclidean time (t_2) for $m_\pi^2 = 0.4854$ GeV^2, the SU(3)-flavor limit. The lines indicate the fitting windows and the best fit value.
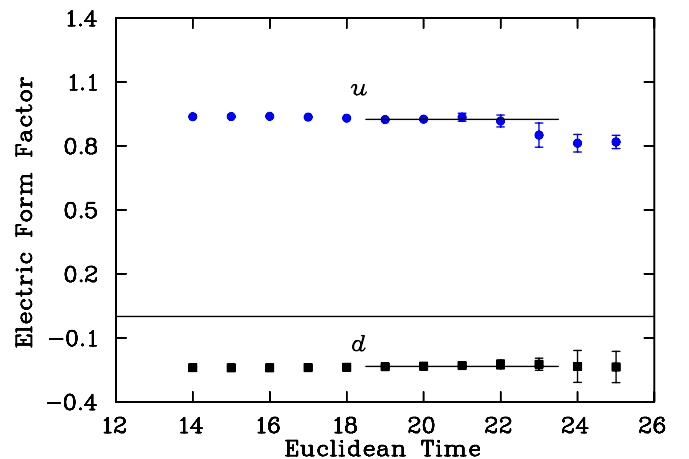

FIG. 4 (color online).   Quark-sector contributions (including charge and quark number factors) to the electric form factor of the proton at $Q^2 = 0.227(2)$ (GeV^2) as a function of Euclidean time, t_2, for the ninth quark mass where $m_\pi^2 = 0.2153(35)$ GeV^2. The correlator is obtained from the splitting between the ninth and eighth quark-mass states. The lines indicate the fitting windows and the best fit value.

TABLE II. Quark-sector contributions to the electric form factors of the nucleon at $Q^2 = 0.227(2)$ GeV^2. Sector contributions are for a single quark having unit charge. The fit windows are selected using the criteria outlined in Sec. III D.

m_π^2 (GeV^2)	u_p			d_p		
	Fit value	Fit window	χ^2/d.o.f.	Fit value	Fit window	χ^2/d.o.f.
0.9972(55)	0.798(5)	21–25	1.02	0.805(4)	21–25	2.36
0.8947(54)	0.789(5)	21–25	0.89	0.796(5)	21–25	2.53
0.7931(53)	0.779(6)	21–25	0.64	0.788(5)	21–25	2.21
0.6910(35)	0.768(6)	21–25	0.86	0.780(5)	21–25	1.57
0.5925(33)	0.756(7)	21–25	0.80	0.769(6)	21–25	1.42
0.4854(31)	0.740(9)	21–25	0.62	0.755(9)	21–25	1.19
0.3795(31)	0.725(10)	19–23	1.23	0.741(11)	19–23	0.78
0.2839(33)	0.708(12)	19–23	1.37	0.723(14)	19–23	1.31
0.2153(35)	0.693(15)	19–23	0.82	0.700(20)	19–23	1.23
0.1384(43)	0.682(17)	16–20	1.02	0.678(25)	16–20	0.89
0.0939(44)	0.666(25)	16–19	1.47	0.644(38)	16–19	1.28

TABLE III. Quark-sector contributions to the electric form factors of Σ baryons at $Q^2 = 0.227(2)$ GeV^2. Sector contributions are for a single quark having unit charge. The fit windows are selected using the criteria outlined in Sec. III D.

m_π^2 (GeV^2)	u_Σ or d_Σ			s_Σ		
	Fit value	Fit window	χ^2/d.o.f.	Fit value	Fit window	χ^2/d.o.f.
0.9972(55)	0.793(6)	21–25	0.91	0.759(6)	21–25	1.70
0.8947(54)	0.785(7)	21–25	0.86	0.758(7)	21–25	1.71
0.7931(53)	0.776(7)	21–25	0.66	0.757(8)	21–25	1.59
0.6910(35)	0.766(6)	21–25	1.00	0.757(6)	21–25	1.40
0.5925(33)	0.755(7)	21–25	0.90	0.756(7)	21–25	1.36
0.4854(31)	0.740(9)	21–25	0.62	0.755(9)	21–25	1.19
0.3795(31)	0.726(10)	19–23	1.46	0.754(10)	19–23	0.37
0.2839(33)	0.711(12)	19–23	1.78	0.753(11)	19–23	0.58
0.2153(35)	0.700(14)	19–23	0.73	0.752(13)	19–23	0.39
0.1384(43)	0.680(18)	19–21	0.73	0.754(17)	19–21	0.18
0.0939(44)	0.670(23)	19–23	1.30	0.750(26)	19–21	1.40

TABLE IV. Quark-sector contributions to the electric form factors of Λ at $Q^2 = 0.227(2)$ GeV^2. Sector contributions are for a single quark having unit charge. The fit windows are selected using the criteria outlined in Sec. III D.

m_π^2 (GeV^2)	u_Λ or d_Λ			s_Λ		
	Fit value	Fit window	χ^2/d.o.f.	Fit value	Fit window	χ^2/d.o.f.
0.9972(55)	0.803(5)	21–25	1.20	0.754(8)	21–25	0.64
0.8947(54)	0.794(6)	21–25	1.23	0.744(9)	21–25	0.58
0.7931(53)	0.785(7)	21–25	1.06	0.744(10)	21–25	0.54
0.6910(35)	0.775(6)	21–25	1.17	0.738(8)	21–25	0.55
0.5925(33)	0.765(7)	21–25	1.12	0.737(9)	21–25	0.48
0.4854(31)	0.750(8)	21–25	1.02	0.735(10)	21–25	0.49
0.3795(31)	0.736(9)	19–23	0.94	0.734(11)	19–23	0.88
0.2839(33)	0.720(11)	19–23	1.17	0.730(12)	19–23	1.05
0.2153(35)	0.704(13)	19–23	1.23	0.727(13)	19–23	0.55
0.1384(43)	0.694(13)	16–18	2.07	0.727(13)	16–18	0.62
0.0939(44)	0.686(13)	16–18	1.22	0.729(14)	16–18	0.29

TABLE V. Quark-sector contributions to the electric form factors of Ξ baryons at $Q^2 = 0.227(2)$ GeV^2. Sector contributions are for a single quark having unit charge. The fit windows are selected using the criteria outlined in Sec. III D.

m_π^2 (GeV^2)	s_Ξ			u_Ξ or d_Ξ		
	Fit value	Fit window	χ^2/d.o.f.	Fit value	Fit window	χ^2/d.o.f.
0.9972(55)	0.747(9)	21–25	0.34	0.804(8)	21–25	1.60
0.8947(54)	0.747(9)	21–25	0.36	0.794(8)	21–25	1.53
0.7931(53)	0.746(10)	21–25	0.37	0.785(9)	21–25	1.52
0.6910(35)	0.742(8)	21–25	0.54	0.778(7)	21–25	1.38
0.5925(33)	0.741(8)	21–25	0.55	0.768(8)	21–25	1.24
0.4854(31)	0.740(9)	21–25	0.62	0.755(9)	21–25	1.19
0.3795(31)	0.739(9)	19–23	0.70	0.740(10)	21–25	1.45
0.2839(33)	0.738(10)	19–23	1.18	0.723(13)	21–25	1.22
0.2153(35)	0.736(10)	19–23	1.42	0.709(16)	21–25	0.81
0.1384(43)	0.733(10)	19–23	0.52	0.690(19)	20–23	0.71
0.0939(44)	0.725(11)	19–23	1.21	0.672(22)	20–23	0.59

quark mass where $m_\pi^2 = 0.2153(35)$ GeV^2. Again the early onset of acceptable plateau behavior is apparent here.

Results for the quark-sector contributions to the magnetic form factors of octet baryons are summarized in Tables VI, VII, VIII, and IX.

V. DISCUSSION OF RESULTS

A. Charge radii

To make contact with the extensive phenomenology of the field, our results for the electric form factors are expressed in terms of charge radii. It is well known that the experimentally measured electric (and magnetic) form factor of the proton is described well by a dipole ansatz at small Q^2

$$\mathcal{G}_E(Q^2) = \frac{\mathcal{G}_E(0)}{(1 + Q^2/m^2)^2}; \qquad Q^2 \geq 0, \qquad (5.1)$$

where m characterizes the size of the proton. This behavior has also been observed in recent lattice calculations [12] where many momentum transfers have been considered. Using this observation, together with

$$\langle r_E^2 \rangle = -6 \frac{d}{dQ^2} \mathcal{G}_E(Q^2) \bigg|_{Q^2=0}, \qquad (5.2)$$

we arrive at an expression which allows us to calculate the electric charge radius of a baryon using our two available values of the Sach's electric form factor ($\mathcal{G}_E(Q_{min}^2)$, $\mathcal{G}_E(0)$), namely
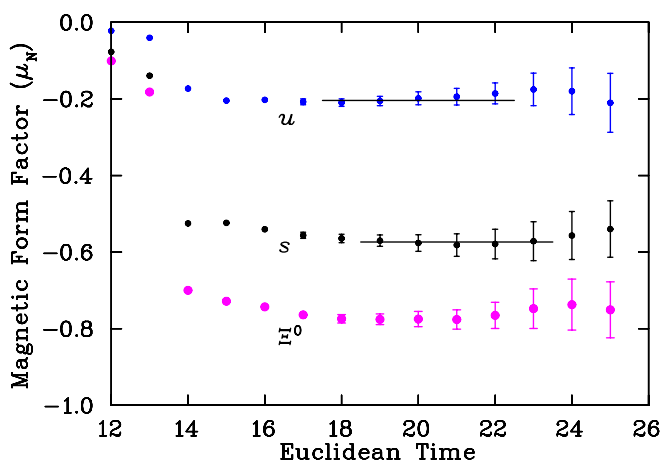

FIG. 5 (color online). Magnetic form factors of Ξ^0 and its quark sectors (including charge and quark number factors) at $Q^2 = 0.227(2)$ GeV^2 as a function of Euclidean time (t_2) for $m_\pi^2 = 0.4854$ GeV^2, the SU(3)-flavor limit. The lines indicate the fitting windows and the best fit value.
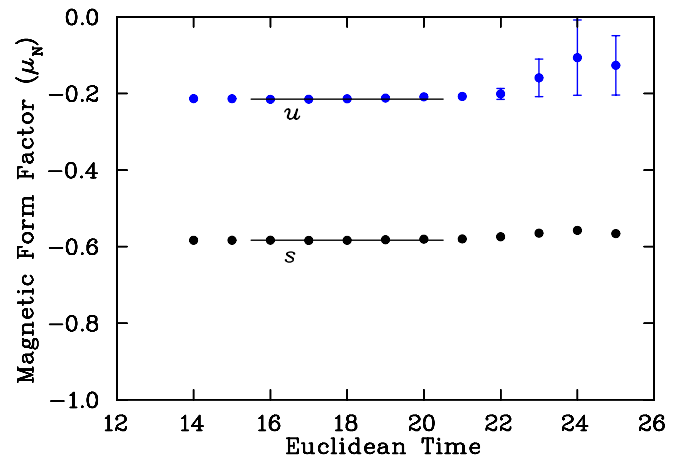

FIG. 6 (color online). Quark-sector contributions (including charge and quark number factors) to the magnetic form factor of Ξ^0 at $Q^2 = 0.227(2)$ (GeV^2) as a function of Euclidean time, t_2, for the ninth quark mass where $m_\pi^2 = 0.2153(35)$ GeV^2. The correlator is obtained from the splitting between the ninth and eighth quark-mass states. The lines indicate the fitting windows and the best fit value.

TABLE VI.   Quark-sector contributions to the magnetic form factors of the nucleon at $Q^2 = 0.227(2)$ GeV^2. Sector contributions are for a single quark having unit charge. The fit windows are selected using the criteria outlined in Sec. III D.

m_π^2 (GeV^2)	u_p (μ_N)			d_p (μ_N)		
	Fit value	Fit window	χ^2/d.o.f.	Fit value	Fit window	χ^2/d.o.f.
0.9972(55)	0.765(12)	19–23	1.78	−0.295(7)	18–22	0.61
0.8947(54)	0.785(14)	19–23	1.33	−0.298(8)	18–22	0.51
0.7931(53)	0.804(16)	19–23	1.01	−0.301(9)	18–22	0.43
0.6931(51)	0.817(13)	19–23	1.00	−0.301(8)	18–22	0.91
0.5944(51)	0.838(15)	19–23	0.73	−0.304(10)	18–22	0.79
0.4869(50)	0.861(20)	19–23	0.64	−0.306(12)	18–22	0.86
0.3795(31)	0.893(24)	17–21	0.14	−0.314(14)	16–18	1.64
0.2839(33)	0.932(31)	17–21	0.14	−0.313(19)	16–19	1.24
0.2153(35)	0.967(42)	17–21	0.61	−0.313(31)	16–20	0.53
0.1384(43)	1.034(52)	16–20	1.12	−0.309(40)	15–19	0.49
0.0939(44)	1.024(72)	15–17	0.82	−0.336(54)	15–19	1.47

TABLE VII.   Quark-sector contributions to the magnetic form factors of Σ baryons at $Q^2 = 0.227(2)$ GeV^2. Sector contributions are for a single quark having unit charge. The fit windows are selected using the criteria outlined in Sec. III D.

m_π^2 (GeV^2)	u_Σ or d_Σ (μ_N)			s_Σ (μ_N)		
	Fit value	Fit window	χ^2/d.o.f.	Fit value	Fit window	χ^2/d.o.f.
0.9972(55)	0.775(14)	19–23	1.22	−0.316(10)	18–22	0.73
0.8947(54)	0.793(16)	19–23	1.10	−0.314(11)	18–22	0.63
0.7931(53)	0.810(18)	19–23	0.96	−0.312(11)	18–22	0.55
0.6910(35)	0.821(14)	19–23	0.98	−0.309(9)	18–22	0.94
0.5925(33)	0.840(16)	19–23	0.82	−0.308(10)	18–22	0.86
0.4854(31)	0.861(20)	19–23	0.64	−0.306(12)	18–22	0.86
0.3795(31)	0.886(23)	17–21	0.19	−0.308(13)	16–18	0.42
0.2839(33)	0.914(27)	17–21	0.26	−0.310(15)	16–18	0.03
0.2153(35)	0.941(32)	17–21	0.61	−0.317(19)	16–18	0.04
0.1384(43)	0.964(33)	15–20	1.57	−0.317(24)	16–18	0.92
0.0939(44)	0.969(41)	15–17	0.11	−0.322(28)	16–18	1.08

TABLE VIII.   Quark-sector contributions to the magnetic form factors of Λ at $Q^2 = 0.227(2)$ GeV^2. Sector contributions are for a single quark having unit charge. The fit windows are selected using the criteria outlined in Sec. III D.

m_π^2 (GeV^2)	u_Λ or d_Λ (μ_N)			s_Λ (μ_N)		
	Fit value	Fit window	χ^2/d.o.f.	Fit value	Fit window	χ^2/d.o.f.
0.9972(55)	0.069(9)	19–23	1.26	1.200(22)	18–22	1.38
0.8947(54)	0.072(9)	19–23	1.20	1.210(22)	18–22	1.17
0.7931(53)	0.075(10)	19–23	1.07	1.214(24)	18–22	0.99
0.6910(35)	0.079(8)	19–23	1.08	1.217(17)	18–22	0.95
0.5925(33)	0.083(9)	19–23	1.00	1.228(18)	18–22	0.80
0.4854(31)	0.087(11)	19–23	0.88	1.241(21)	18–22	0.75
0.3795(31)	0.091(12)	17–21	0.55	1.259(22)	16–20	0.59
0.2839(33)	0.097(13)	17–21	0.29	1.277(25)	16–20	0.42
0.2153(35)	0.099(17)	17–21	0.36	1.293(28)	16–20	0.42
0.1384(43)	0.106(19)	15–17	1.23	1.308(33)	16–18	0.94
0.0939(44)	0.105(22)	15–17	0.67	1.314(37)	15–17	1.06

TABLE IX. Quark-sector contributions to the magnetic form factors of Ξ baryons at $Q^2 = 0.227(2)$ GeV^2. Sector contributions are for a single quark having unit charge. The fit windows are selected using the criteria outlined in Sec. III D.

m_π^2 (GeV^2)	s_Ξ (μ_N)			u_Ξ or d_Ξ (μ_N)		
	Fit value	Fit window	χ^2/d.o.f.	Fit value	Fit window	χ^2/d.o.f.
0.9972(55)	0.846(27)	19–23	0.60	−0.290(10)	18–22	0.19
0.8947(54)	0.849(27)	19–23	0.67	−0.294(11)	18–22	0.21
0.7931(53)	0.851(28)	19–23	0.75	−0.299(12)	18–22	0.21
0.6931(51)	0.855(19)	19–23	0.41	−0.300(10)	18–22	0.59
0.5944(51)	0.858(19)	19–23	0.49	−0.303(11)	18–22	0.68
0.4869(50)	0.861(20)	19–23	0.64	−0.306(12)	18–22	0.86
0.3795(31)	0.866(21)	16–20	0.84	−0.311(13)	16–20	1.77
0.2839(33)	0.871(21)	16–20	0.78	−0.316(14)	16–20	1.66
0.2153(35)	0.875(22)	16–20	1.04	−0.322(15)	16–20	0.77
0.1384(43)	0.879(22)	16–20	1.16	−0.328(17)	15–19	0.86
0.0939(44)	0.879(23)	16–20	0.55	−0.333(18)	15–19	1.00

TABLE X. Nucleon electric charge radii squared. Quark-sector contributions are indicated for single quarks having unit charge. Baryon charge states are also summarized. Values for m_π^2 and $\langle r^2 \rangle$ are in units of GeV^2 and fm^2 respectively.

m_π^2	u_p	d_p	p	n
0.9972(55)	0.243(7)	0.231(6)	0.247(8)	−0.007(3)
0.8947(54)	0.256(8)	0.245(7)	0.259(9)	−0.007(3)
0.7931(53)	0.270(9)	0.257(8)	0.273(10)	−0.008(4)
0.6910(35)	0.288(9)	0.270(8)	0.294(10)	−0.012(4)
0.5925(33)	0.307(11)	0.286(10)	0.314(12)	−0.014(5)
0.4854(31)	0.332(14)	0.309(14)	0.340(16)	−0.015(7)
0.3795(31)	0.358(17)	0.332(17)	0.367(19)	−0.017(9)
0.2839(33)	0.389(22)	0.363(24)	0.397(24)	−0.017(12)
0.2153(35)	0.416(27)	0.403(36)	0.420(29)	−0.008(16)
0.1384(43)	0.437(31)	0.445(46)	0.435(32)	0.005(21)
0.0939(44)	0.467(48)	0.510(77)	0.452(53)	0.029(41)

TABLE XI. Σ electric charge radii squared. Quark-sector contributions are indicated for single quarks having unit charge. Baryon charge states are also summarized where absolute values of the Σ^- results are reported. Values for m_π^2 and $\langle r^2 \rangle$ are in units of GeV^2 and fm^2 respectively.

m_π^2	u_Σ or d_Σ	s_Σ	Σ^+	Σ^0	Σ^-
0.9972(55)	0.249(9)	0.301(10)	0.232(10)	−0.017(3)	0.266(9)
0.8947(54)	0.261(10)	0.302(11)	0.249(12)	−0.013(3)	0.275(9)
0.7931(53)	0.276(11)	0.304(12)	0.266(15)	−0.010(3)	0.285(11)
0.6910(35)	0.291(10)	0.304(10)	0.286(11)	−0.005(2)	0.295(9)
0.5925(33)	0.309(11)	0.306(11)	0.310(13)	0.001(3)	0.308(11)
0.4854(31)	0.332(14)	0.309(14)	0.340(16)	0.008(4)	0.324(13)
0.3795(31)	0.356(16)	0.310(15)	0.371(19)	0.015(4)	0.341(15)
0.2839(33)	0.382(20)	0.312(18)	0.405(23)	0.023(5)	0.359(18)
0.2153(35)	0.401(25)	0.315(21)	0.430(29)	0.029(6)	0.372(22)
0.1384(43)	0.438(33)	0.311(26)	0.480(38)	0.042(8)	0.395(28)
0.0939(44)	0.456(43)	0.318(41)	0.503(54)	0.046(15)	0.410(37)

TABLE XII. Λ electric charge radii squared. Quark-sector contributions are indicated for single quarks having unit charge. The baryon charge state is also provided. Values for m_π^2 and $\langle r^2 \rangle$ are in units of GeV^2 and fm^2 respectively.

m_π^2	u_Λ or d_Λ	s_Λ	Λ^0
0.9972(55)	0.235(8)	0.322(13)	−0.029(3)
0.8947(54)	0.248(9)	0.323(14)	−0.025(3)
0.7931(53)	0.262(10)	0.324(15)	−0.021(3)
0.6910(35)	0.276(9)	0.335(13)	−0.020(3)
0.5925(33)	0.293(10)	0.336(14)	−0.014(3)
0.4854(31)	0.316(13)	0.340(16)	−0.008(4)
0.3795(31)	0.340(15)	0.343(18)	−0.001(4)
0.2839(33)	0.367(18)	0.350(19)	0.006(5)
0.2153(35)	0.395(23)	0.357(22)	0.013(6)
0.1384(43)	0.414(24)	0.356(22)	0.019(6)
0.0939(44)	0.428(25)	0.354(23)	0.025(7)

$$\frac{\langle r_E^2 \rangle}{\mathcal{G}_E(0)} = \frac{12}{Q^2}\left(\sqrt{\frac{\mathcal{G}_E(0)}{\mathcal{G}_E(Q^2)}} - 1\right). \tag{5.3}$$

While Eq. (5.1) is suitable for a charged baryon, alternative forms must be considered for neutral baryons where $\mathcal{G}_E(0) = 0$.

However, we have direct access to the charge distributions of the individual quark sectors, a subject receiving tremendous experimental attention in the search for the role of hidden flavor in baryon structure. In this case Eq. (5.3) may be applied to each quark sector providing an opportunity to determine the charge radii on a sector by sector basis.

For neutral baryons it becomes a simple matter to construct the charge radii by first calculating the charge radii for each quark sector. These quark sectors are then combined using the appropriate charge and quark number factors as described in Sec. IV B to obtain the total baryon charge radii. Indeed, all baryon charge radii, including the charged states, are calculated in this manner.

Tables X, XI, XII, and XIII provide the electric charge radii of the octet baryons and their quark-sector contributions normalized to the case of single quarks with unit charge.

1. Quenched chiral perturbation theory

The effective field theory formalism of quenched chiral perturbation theory (QχPT) predicts significant contributions to the charge radii which have their origin in virtual meson-baryon loop transitions. These loops give rise to contributions which have a nonanalytic dependence on the quark mass or squared pion mass. While the absence of sea-quark loops generally acts to suppress the magnitude of the coefficients of these terms (and occasionally the sign is reversed), there are several channels in which these contributions remain significant.

The leading nonanalytic (LNA) and next-to-leading nonanalytic (NLNA) behavior of charge distribution radii in full QCD are

$$\langle r_E^2 \rangle = \frac{1}{16\pi^2 f^2}\sum_i\left[5\beta_i \log\left(\frac{m_i^2}{\mu^2}\right) - 10\beta_i' \mathcal{G}(m_i, \Delta, \mu)\right.$$
$$\left. + c_0 + c_2 m_i^2 + c_4 m_i^4 \dots\right]. \tag{5.4}$$

Here the sum over i includes the π and K pseudoscalar mesons. The contributions of the various charge states of these mesons are contained in the coefficients β and β', reflecting electric charge and SU(3) axial couplings, D, F and C. In quenching the theory, the coefficients β and β' are modified to reflect the absence of sea-quark loops.

The first term arises from octet baryon to octet-baryon—meson transitions. Thus charge radii are characterized by a logarithmic divergence [36] in the chiral limit ($m_\pi^2 \rightarrow 0$). In this simple form, the mass splittings between baryon-octet members is neglected.

TABLE XIII. Ξ electric charge radii squared. Quark-sector contributions are indicated for single quarks having unit charge. Baryon charge states are also summarized where absolute values of the Ξ^- results are reported. Values for m_π^2 and $\langle r^2 \rangle$ are in units of GeV^2 and fm^2 respectively.

m_π^2	s_Ξ	u_Ξ or d_Ξ	Ξ^-	Ξ^0
0.9972(55)	0.319(14)	0.235(11)	0.290(12)	−0.056(7)
0.8947(54)	0.320(15)	0.249(12)	0.296(13)	−0.047(7)
0.7931(53)	0.322(16)	0.262(13)	0.301(14)	−0.039(8)
0.6910(35)	0.329(13)	0.273(11)	0.310(11)	−0.037(6)
0.5925(33)	0.330(14)	0.288(12)	0.316(12)	−0.028(7)
0.4854(31)	0.332(14)	0.309(14)	0.324(13)	−0.015(7)
0.3795(31)	0.334(15)	0.333(17)	0.334(14)	−0.0003(80)
0.2839(33)	0.337(15)	0.361(21)	0.345(16)	0.016(10)
0.2153(35)	0.340(16)	0.385(27)	0.355(18)	0.029(13)
0.1384(43)	0.345(16)	0.419(34)	0.370(19)	0.049(19)
0.0939(44)	0.358(18)	0.451(41)	0.389(23)	0.062(22)

The second term of Eq. (5.4) arises from octet baryon to decuplet-baryon—meson transitions. As the splitting between the baryon octet and decuplet does not vanish in the chiral limit, the mass splitting, $\Delta = M_\Delta - M_N$, between the nucleon and Δ for example, plays an important role. The function $\mathcal{G}(m_i, \Delta, \mu)$ is

$$\mathcal{G}(m, \Delta, \mu) = \log\left(\frac{m_i^2}{\mu^2}\right) - \frac{\Delta}{\sqrt{\Delta^2 - m_i^2}}$$

$$\times \log\frac{\Delta - \sqrt{\Delta^2 - m_i^2 + i\epsilon}}{\Delta + \sqrt{\Delta^2 - m_i^2 + i\epsilon}}. \qquad (5.5)$$

As the tadpole graph contributing to the LNA term of charge radii in full QCD vanishes in quenched QCD [37], the coefficients β and β' for charge radii are identical to those for magnetic moments in quenched QCD [15,16]. Figure 7 displays the nonanalytic contributions from QχPT as given in Eq. (5.4), plotted for the sample case of the proton. In this case, the values of β and β' are $-\frac{4}{3}D^2$ and $-\frac{1}{6}C^2$ respectively [15,16]. Here the axial couplings D and C are related by $C = 2D$ and D is taken as 0.76. The scale μ^2 is taken to be 1 GeV^2 and serves only to define c_0.

Because these nonanalytic contributions are complemented by terms analytic in the quark mass or pion-mass squared, the slope and curvature at large m_π^2 of these contributions is not significant. What is significant is the curvature at small m_π^2 and we see that this curvature is dominated by the LNA term. Here there is no mass splitting to mask the effects of dynamical chiral symmetry breaking. Thus, we will examine the extent to which our simulation results are consistent with the LNA behavior of QχPT.
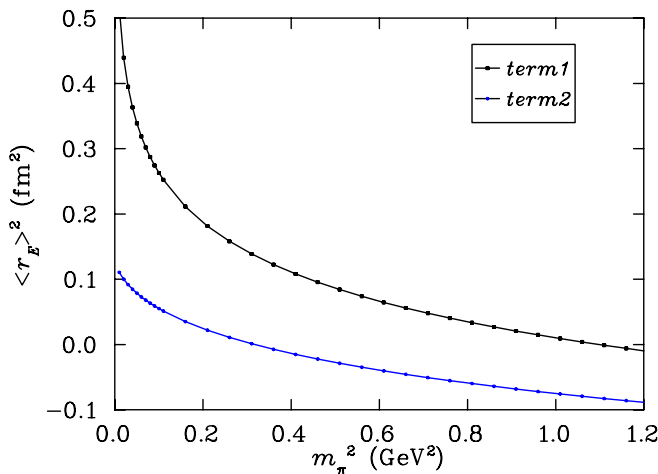
FIG. 7 (color online).   The leading (upper curve) and next-to-leading (lower curve) nonanalytic contributions to the charge radius of the proton as given by quenched chiral perturbation theory in Eq. (5.4).

The coefficient β is related to the coefficient of the leading nonanalytic (LNA) contribution to the magnetic moment, χ, via the relation [15]

TABLE XIV.   Coefficients, χ, providing the LNA contribution to baryon magnetic moments and charge radii in quenched QCD. Coefficients for magnetic moments in full QCD are also indicated. Here the coefficients for quark-sector contributions to baryon properties are indicated for quarks having unit charge. Note that u_p for example denotes the coefficient for the two u quarks of the proton, each of which have unit charge. Intermediate (Int.) meson-baryon channels are indicated to allow for SU(3)-flavor breaking in both the meson and baryon masses. The coefficients are calculated from the expressions of Ref. [15] with the axial couplings $F = 0.50$ and $D = 0.76$ with $f_\pi = 93$ MeV.

q	Int.	Full QCD	Quenched QCD
$u_p \mid d_n$	$N\pi$	-6.87	-3.33
	ΛK	-3.68	0
	ΣK	-0.15	0
$d_p \mid u_n$	$N\pi$	$+6.87$	$+3.33$
	ΣK	-0.29	0
$s_p \mid s_n$	ΛK	$+3.68$	0
	ΣK	$+0.44$	0
$u_{\Sigma^+} \mid d_{\Sigma^-}$	$\Sigma\pi$	-2.16	0
	$\Lambda\pi$	-1.67	0
	NK	0	-0.29
	ΞK	-6.87	-3.04
$d_{\Sigma^+} \mid u_{\Sigma^-}$	$\Sigma\pi$	$+2.16$	0
	$\Lambda\pi$	$+1.67$	0
	NK	$+0.29$	0
s_Σ	NK	-0.29	$+0.29$
	ΞK	$+6.87$	$+3.04$
	$\Sigma\eta_s$	0	0
$u_{\Sigma^0} \mid d_{\Sigma^0}$	$\Sigma\pi$	0	0
	$\Lambda\pi$	0	0
	NK	$+0.15$	-0.15
	ΞK	-3.43	-1.52
$u_\Lambda \mid d_\Lambda$	$\Sigma\pi$	0	0
	$\Lambda\eta_l$	0	0
	NK	$+3.68$	$+1.23$
	ΞK	-0.40	$+0.44$
s_Λ	$\Lambda\eta_s$	0	0
	NK	-7.36	-2.45
	ΞK	$+0.79$	-0.88
$u_{\Xi^0} \mid d_{\Xi^-}$	$\Xi\pi$	-0.29	0
	ΛK	0	-0.40
	ΣK	$+6.87$	$+3.43$
	ΩK	0	$+0.29$
$d_{\Xi^0} \mid u_{\Xi^-}$	$\Xi\pi$	$+0.29$	0
	ΛK	$+0.40$	0
	ΣK	$+3.43$	0
s_Ξ	ΛK	-0.40	$+0.40$
	ΣK	-10.3	-3.43
	ΩK	0	-0.29
	$\Xi\eta_s$	0	0

$$\beta \frac{m_N}{8\pi f_\pi^2} = \chi. \qquad (5.6)$$

The coefficients χ have been determined for octet baryons and their individual quark-sector contributions in Ref. [15] and numerical values are reproduced in Tables XIV and XV for ready reference.

Since $m_\pi^2 < 1$ GeV^2 in our simulations, the logarithmic term is negative for all quark masses considered here. Hence, the charge radius will exhibit a logarithmic diver-

TABLE XV. Coefficients, χ, providing the LNA contribution to baryon magnetic moments and charge radii in quenched QCD. Coefficients for magnetic moments in full QCD are also indicated. Intermediate (Int.) meson-baryon channels are indicated to allow for SU(3)-flavor breaking in both the meson and baryon masses. The coefficients are calculated from the expressions of Ref. [15] with the axial couplings $F = 0.50$ and $D = 0.76$ with $f_\pi = 93$ MeV.

Baryon	Channel	Full QCD	Quenched QCD
p	$N\pi$	-6.87	-3.33
	ΛK	-3.68	0
	ΣK	-0.15	0
n	$N\pi$	$+6.87$	$+3.33$
	ΛK	0	0
	ΣK	-0.29	0
Σ^+	$\Sigma\pi$	-2.16	0
	$\Lambda\pi$	-1.67	0
	NK	0	-0.29
	ΞK	-6.87	-3.04
	$\Sigma\eta_s$	0	0
Σ^0	$\Sigma\pi$	0	0
	$\Lambda\pi$	0	0
	NK	$+0.15$	-0.15
	ΞK	-3.43	-1.52
	$\Sigma\eta_s$	0	0
Σ^-	$\Sigma\pi$	$+2.16$	0
	$\Lambda\pi$	$+1.67$	0
	NK	$+0.29$	0
	ΞK	0	0
	$\Sigma\eta_s$	0	0
Λ	$\Sigma\pi$	0	0
	$\Lambda\eta_l$	0	0
	NK	$+3.68$	$+1.23$
	ΞK	-0.40	$+0.44$
	$\Lambda\eta_s$	0	0
Ξ^0	$\Xi\pi$	-0.29	0
	ΛK	0	-0.40
	ΣK	$+6.87$	$+3.43$
	ΩK	0	$+0.29$
	$\Xi\eta_s$	0	0
Ξ^-	$\Xi\pi$	$+0.29$	0
	ΛK	$+0.40$	0
	ΣK	$+3.43$	0
	ΩK	0	0
	$\Xi\eta_s$	0	0

gence in chiral limit to either positive or negative infinity, depending on the whether β (or χ) is negative or positive, respectively.

In the quenched approximation, the flavor-singlet η' meson remains degenerate with the pion and makes important contributions to quenched chiral nonanalytic behavior. The neutrality of its charge prevents it from contributing to the coefficients of Tables XIV and XV. However, the double hair-pin diagram in which the vector current couples to the virtual baryon intermediary does give rise to chirally-singular behavior. However the relatively small couplings render these contributions small at the quark masses probed here.

2. Quark-sector charge radii

We begin with an examination of the quark contributions to baryon charge radii. The results are reported for single quarks of unit charge. Of particular interest are the contributions of similar quarks experiencing different environments. Traditionally, quark models of hadron structure neglected such environment sensitivity. However, such environment sensitivity is manifest in chiral effective field theory. The finite kaon mass in the chiral limit renders the kaon's contributions to curvature almost trivial relative to the pion.

Figure 8 displays the charge radii of the u-quark distribution in the proton and compares this with the u-quark distribution in Σ^+. The SU(3)-flavor limit is manifest at $m_\pi^2 \sim 0.5$ GeV^2. The replacement of a d quark in the proton, by an s quark in Σ^+ gives rise to only a small environment sensitivity in the u-quark properties.

Referring to the chiral coefficients of Table XIV, the negative value of χ for u_p indicates that the charge radius of the u quark distribution in the proton should diverge to
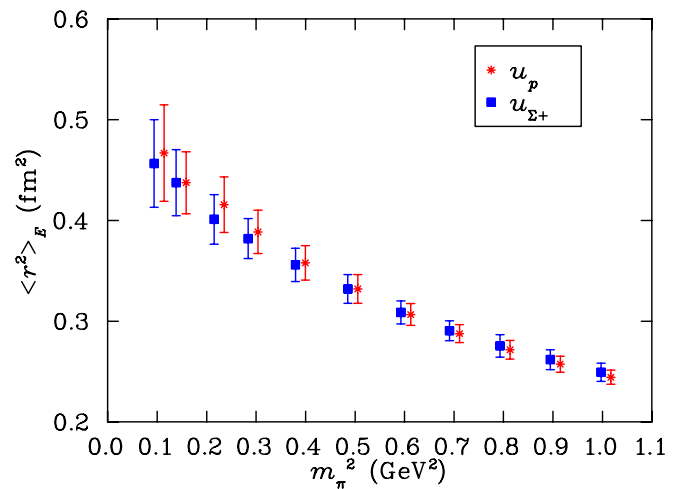

FIG. 8 (color online). Electric charge radii of the u-quark distribution in the proton, u_p, and Σ^+, u_{Σ^+}, as a function of m_π^2 representing the quark masses considered in the simulation. The results for u_p are offset for clarity.

positive infinity in the chiral limit. A physical understanding of this is made obvious by considering the virtual transition $p \rightarrow n\pi^+$, which at the quark level can be understood as $(uud) \rightarrow (udd)(\bar{d}u)$. In the chiral limit, the π^+ carries the u quark to infinity such that u-quark charge distribution radius in the proton diverges.

In the case of the u quark in Σ^+, the coefficient of the logarithmic divergence is zero in the π channel and hence no divergence is expected. While there is a significant coefficient for transitions to ΞK, the increased mass of the Ξ baryon makes this channel unfavorably suppressed.

The results in Fig. 8 for u_p exhibit an upward trend and increasing curvature with reducing quark mass. The u_{Σ^+} rises more slowly. The statistical significance of the difference in u-quark distributions is illustrated in Fig. 9. Hence these results are in qualitative agreement with the LNA expectations of chiral effective field theory.

Figure 10 displays the electric charge radii of the u quark in the neutron (u_n) and in Ξ^0 (u_{Ξ^0}) as a function of m_π^2. Here we observe that the charge radii of u_n and u_{Ξ^0} are nearly equal at heavy-quark masses, but in the chiral limit some evidence of environment sensitivity is revealed. The light d-quark environment of the u quark in the neutron provides enhanced chiral curvature as the chiral limit is approached. Figure 11 illustrates the correlated difference of u-quark distributions, where the effect is seen to be at the one-sigma border of statistical significance.

However, the true nature of the underlying physics is much more subtle. From Table XIV, we see that the quenched coefficient (last column) for the u quark in the neutron is positive in the π channel, from which we can deduce that the charge radius should actually diverge to negative infinity in the chiral limit.

Physically this can be understood by looking at the quark contributions to the virtual transition $n \rightarrow p\pi^-$ which gives rise to this divergence. In this case one has

FIG. 10 (color online). Charge radii of u_n and u_{Ξ^0} as a function of m_π^2. The data for the u_n are offset for clarity.

$(ddu) \rightarrow (duu)(\bar{u}d)$. In the chiral limit, the mass of the pion approaches zero such that the π^- carries a $\bar{u}$ quark to infinity. Since the d quark is ignored while calculating the u quark contribution (i.e. the electric charge of the d quark may be thought of as zero), the entire charge of the pion comes from the $\bar{u}$ quark, thus taking the u-quark charge distribution radius to negative infinity. However, Fig. 10 shows no such trend.

The coefficient χ for u_{Ξ^0} is zero in the π channel, indicating that there should be no logarithmic divergence in the chiral limit. However it does have a substantial positive coefficient in the favorable ΣK channel, indicating the possibility of downward curvature as the chiral limit is approached. Again, Fig. 10 shows no hint of downward curvature.

While the statistical error bars are sufficiently large to hide such a turn over, there are other interpretations. One possibility is that we are not yet in the true chiral regime
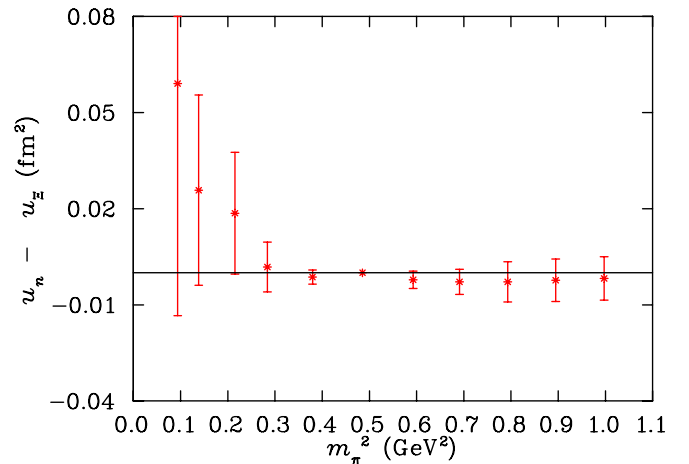

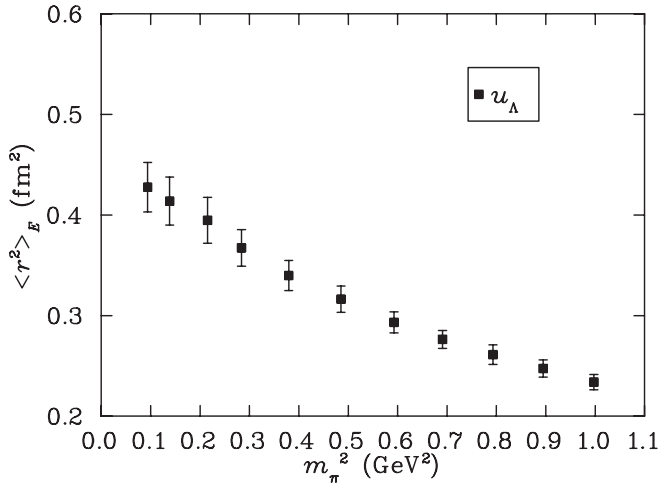FIG. 9 (color online). Correlated difference of the u-quark distributions in the proton and Σ^+.

FIG. 11 (color online). Correlated difference of the u-quark distributions in the neutron and Ξ^0.

FIG. 12. Electric charge distribution radius of a u quark in Λ as a function of m_π^2.

FIG. 13 (color online). Electric charge distribution radii of strange quarks including s_Λ, s_{Ξ^0} and s_{Σ^0}. The data for s_{Ξ^0} and s_Λ are plotted at shifted m_π^2 values for clarity.

where such physics is manifest. Indeed, the divergence of the u-quark charge distribution to negative infinity may only reveal itself at quark masses *lighter* than the physical quark masses.

Alternatively, one might regard this particular case to be somewhat exceptional. It is the only channel in which chiral-loop physics is expected to oppose the natural broadening of a distribution's Compton wavelength. On the lattice, the finite volume restricts the low momenta of the effective field theory to discrete values. It may be that this lattice artifact prevents one from building up sufficient strength in the loop integral to counter the Compton broadening. In this case it would be impossible to observe the divergence of $u_n \to -\infty$ at any quark mass. It will be interesting to resolve this discrepancy with quantitative effective field theory calculations.

Figure 12 reports our results for the charge distribution radius of a u quark in Λ as a function of m_π^2. The chiral coefficient for this is zero in the π channel and hence no divergence is expected. However, there is significant strength for downward curvature in the energetically favorable NK channel. But still, *curvature* associated with K dressings will be subtle. Indeed, the approach to the chiral limit is remarkably linear and contrasts the upward curvature observed for other light-quark flavors. Hence our results are in qualitative agreement with the expectations of QχPT.

Figure 13 illustrates the charge distribution radius of strange quarks in Λ^0, Ξ^0 and Σ^0 and Fig. 14 displays differences in these distributions. In our simulations the strange-quark mass is held fixed and therefore any variation observed in the results is purely environmental in origin. All three distributions suggest a gentle dependence on the mass of the environmental light quarks.

However, the environmental flavor-symmetry dependence of the strange-quark distributions is absolutely remarkable. When the environmental quarks are in an isospin
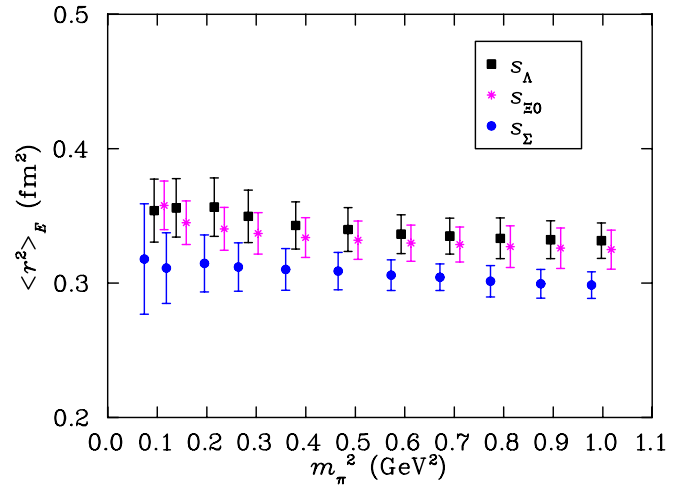
0 state in the Λ, the strange-quark distribution is broad. On the other hand, when the environmental quarks are in an isospin 1 state in Σ baryons, the distribution radius is significantly smaller.

In the case of strange-quark distributions, the LNA contributions are exclusively from transitions involving the kaon. Therefore significant curvature is not expected. On the other hand, one might expect broader distributions in cases where a virtual transition is possible in quenched QCD. Referring to Table XIV, one sees that both s_Λ and s_Ξ have strong transitions to the energetically favorable KN and $K\Sigma$ channels, respectively. The coefficients are negative such that the virtual transitions will act to enhance the charge distributions. This is not the case for s_Σ where the sign is positive and the transition is to the energetically unfavored $K\Xi$ channel. In summary, broader distributions
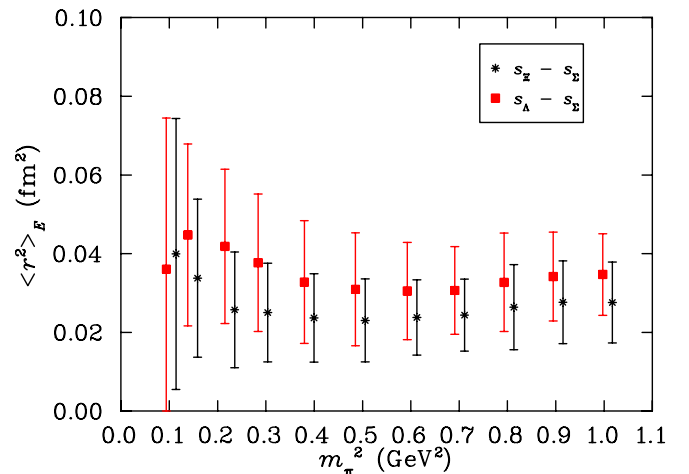

FIG. 14 (color online). Correlated differences of the electric charge distribution radii of strange quarks in Λ, Ξ^0, and Σ^0.

are observed in cases where a virtual transition is possible in QχPT, and this is particularly evident in Fig. 14.

3. Baryon charge radii

The flavor-symmetry dependence of *uds*-quark distributions in Σ^0 and Λ^0 is particularly manifest in Fig. 15. Here the interplay between the light-quark sector with effective charge $1/3$ and the strange sector with charge $-1/3$ is revealed.

At the SU(3) flavor-symmetric point ($m_\pi^2 \sim 0.5$ GeV^2) where the strange and light quarks have the same mass and the Λ and Σ are degenerate in mass, neither charge radius is zero. This very nicely reveals different charge distributions for the quark sectors described in the previous section.

In constituent quark models, this flavor dependence would be described in terms of spin-dependent forces. In the Λ^0 where a scalar diquark can form between the non-strange pair, the charge radius is dominated by the broader strange-quark distribution at the SU(3)-flavor-symmetric point. This is contrasted by the Σ^0 where scalar-diquark pairing would occur between strange and nonstrange quarks, acting to constrict the strange-quark distribution in Σ as seen in Fig. 13. In addition, hyperfine repulsion in the non-strange-quark sector leads to a broader distribution for the light quark sector as indicated in Tables XI and XII. As compelling as this discussion is, this line of reasoning suggests the decuplet-baryon states should have broader quark distributions [21] as scalar-diquark clusters do not dominate there. However, preliminary results from an analysis of decuplet-baryon structure on the same lattice configurations explored here [38], do not reveal broader quark distributions. For this reason, we consider our discussion of virtual transitions in the context of effective field theory in the previous section to be a more relevant description of the underlying physics.

Ultimately, as the chiral limit is approached, the light-quark distribution broadens and dominates the charge radii

FIG. 16 (color online). Electric charge radii of charged hyperons. The Ξ^- and Σ^+ are offset to the left and right, respectively, for clarity.

for both baryons. However, the charge distribution of the Σ^0 is much broader and reflects our discussion of the quark-sector contributions. In particular, the LNA contributions of QχPT act to suppress the distribution of u_Λ and enhance s_Λ, whereas the LNA contributions to Σ^0 are relatively suppressed either by having small coefficients or having energetically unfavorable transitions in the kaon channel. This suppression of u_Λ and enhancement s_Λ combines to give a strong net effect of suppressing the charge radius of the Λ^0.

The hyperon charge states, Σ^- and Ξ^- have chiral coefficients which vanish in quenched QCD. Similarly, Σ^+ has no contributions from virtual pion transitions. The one case, where there is a substantial coefficient, is suppressed energetically. Figure 16 displays our simulation results for the electric charge distribution radii of these hyperons as a function of m_π^2. The ordering of the charge
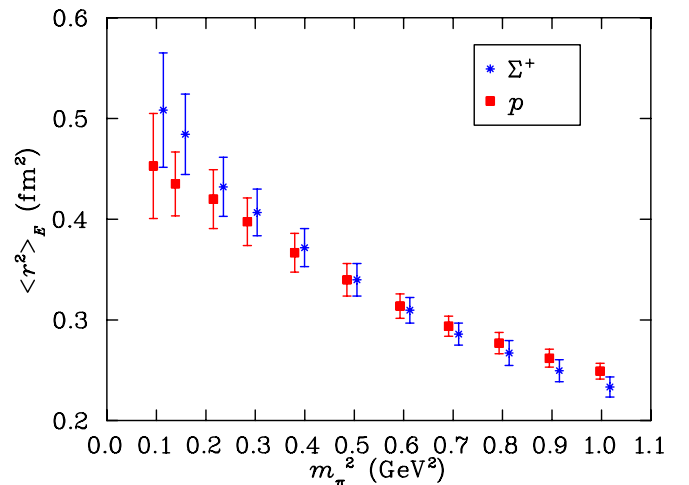

FIG. 15 (color online). Electric charge radii of Σ^0 and Λ^0 as a function of m_π^2. The data for Σ^0 is offset to the right for clarity.

FIG. 17 (color online). Electric charge radii of the proton and Σ^+. Charge radii for Σ^+ are offset for clarity.
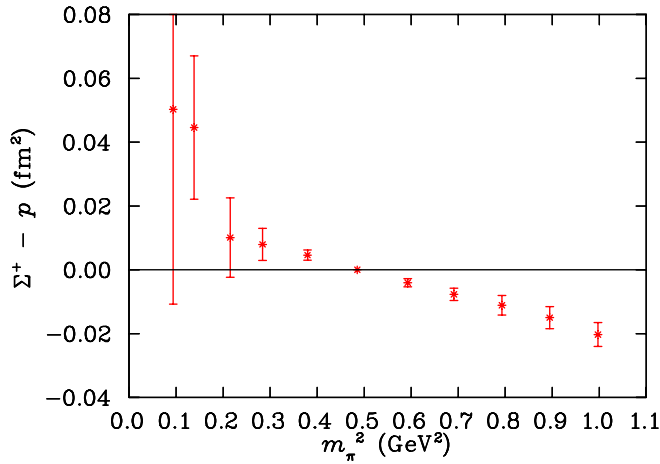
FIG. 18 (color online). Correlated difference of the electric charge radii of the proton and Σ^+.

FIG. 19 (color online). Electric charge radii of the neutron and Ξ^0. Charge radii for the Ξ^0 are shifted to the right for clarity. Asymmetric error bars for the neutron charge radius are described in the text.

radii as the chiral limit is approached is explained by the more localized strange-quark distribution.

Figure 17 compares the charge radii of Σ^+ with the proton. The charge radii of these baryons match at the SU(3) flavor limit where $m_\pi^2 \sim 0.5$ GeV^2 as required. As the chiral limit is approached, the smaller charge distribution of the heavier negatively-charged strange quark acts to make the Σ^+ larger. This is manifest in the simulation results of Fig. 18 illustrating the difference in the charge radii of these baryons. The statistical uncerainties are highly correlated and the signal is revealed in the difference.

While the Σ^+ is not expected to display chiral curvature, the proton charge radius presents one of the more favorable opportunities to observe a hint of the logarithmic divergence to be encountered in the chiral and infinite-volume limits of quenched QCD. However, there is no hint of chiral curvature in favor of the proton over the Σ^+.

The origin of this discrepancy is once again traced to the singly-represented u quark in the neutron, or more specifically in this case, the singly-represented d quark in the proton. As highlighted in the discussion surrounding Fig. 8 and 9 for the splitting, there is a hint of increased curvature for the doubly-represented u quark in the proton over that in Σ, in accord with chiral effective field theory. But this is hidden in the proton charge radius due to the absence of the anticipated curvature of the singly-represented quark in the nucleon, as highlighted in the discussion surrounding Fig. 10.

Similarly, the ultimate divergence of the neutron charge radius to negative infinity via $n \to p\pi^-$ is not yet manifest. Rather a crossing of the central values into positive values of squared charge radii is revealed in Fig. 19. Still, the statistical errors remain consistent with negative values.

The crossing of the central values of the squared neutron charge radius into positive values led us to further examine our selection of fit regime in our correlation-function
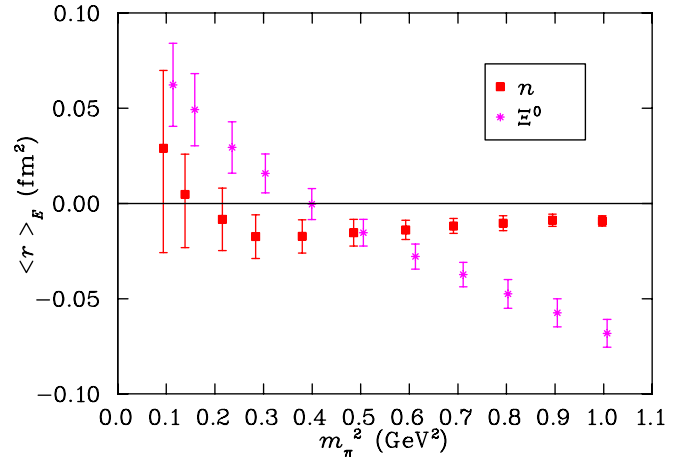
analysis. Our concern is that noise in the correlation function may be distorting the fit. Hence, we have also considered fits including $t = 15$, immediately following the point-split current insertion centered at $t = 14$. While we prefer to allow some Euclidean time evolution following the current insertion, this systematic uncertainty is reflected in the asymmetric error bar of Fig. 19 for the lightest two neutron charge radii.

To summarize, we have explored the electric form factors of the baryon octet and their quark-sector contributions at light-quark masses approaching the chiral regime. The unprecedented nature of our quark masses is illustrated in Fig. 20 which compares the present results for the proton
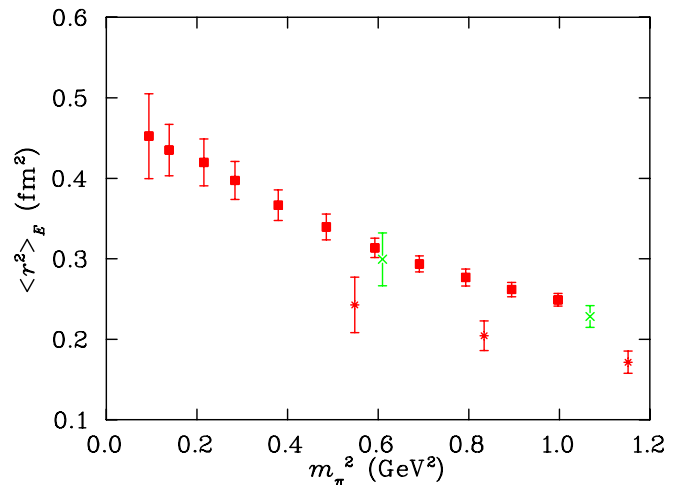

FIG. 20 (color online). The proton charge radius is compared with previous state of the art lattice simulation results in quenched QCD. The solid squares indicate current lattice QCD results with FLIC fermions. The stars indicate the lattice results of [4] while the crosses indicate the results of [5], both of which use the standard Wilson actions for the gauge and fermion fields.

charge radius with the previous state of the art [4,5]. Here the static quark potential has been used to uniformly set the scale among all the results. The small values of the early results are most likely due to the small physical lattice volumes necessitated at that time. The precision afforded by 400 $20^3 \times 40$ lattices is manifest.

We have discovered that all baryons having nonvanishing energetically- favorable couplings to virtual meson-baryon transitions tend to be broader than those which do not. This qualitative realization provides a simple explanation for the patterns revealed in our quenched-QCD simulations.

Still, evidence of chiral *curvature* on our large-volume lattice is rather subtle in general and absent in the exceptional case of the singly-represented quark in the neutron or Ξ. In this case, it is thought that the restriction of momenta to discrete values on the finite-volume lattice prevents the build up of strength in the loop integral of effective field theory. Without sufficient strength, the Compton broadening of the distribution will not be countered as the chiral limit is approached.

B. Magnetic moments

The magnetic moment μ is provided by the magnetic form factor at $Q^2 = 0$, $G_M(0)$, with units of the natural magneton, $\mu_B = e/(2M_B)$, where M_B is the mass of the baryon

$$\mu = G_M(0)\frac{e}{2M_B}. \tag{5.7}$$

While we could present a detailed discussion of the magnetic form factors summarized in Sec. IV B, a more interesting discussion of the results is facilitated via the magnetic moment where chiral nonanalytic behavior takes on a simple functional form and a vast collection of phenomenology is available to provide a context for our results.

Since the magnetic form factors must be calculated at a finite value of momentum transfer, Q^2, the magnetic moment must be inferred from our results, $G_M(Q^2)$, obtained at the minimum nonvanishing momentum transfer available on our periodic lattice. The Q^2 dependence of lattice results from the QCDSF Collaboration [12] are described

TABLE XVI.   Nucleon magnetic moments and their quark-sector contributions. Sector contributions are indicated for single quarks having unit charge. Baryon charge states are also summarized. Values for m_π^2 and magnetic moments are in units of GeV^2 and μ_N respectively.

m_π^2	u_p	d_p	p	n
0.9972(55)	0.960(13)	−0.366(8)	1.401(18)	−0.883(11)
0.8947(54)	0.995(15)	−0.373(9)	1.451(21)	−0.913(12)
0.7931(53)	1.032(18)	−0.382(10)	1.503(25)	−0.943(14)
0.6910(35)	1.064(14)	−0.386(10)	1.547(19)	−0.967(12)
0.5925(33)	1.108(17)	−0.395(12)	1.610(24)	−1.002(15)
0.4854(31)	1.163(24)	−0.406(16)	1.686(33)	−1.046(20)
0.3795(31)	1.231(29)	−0.424(20)	1.783(41)	−1.104(25)
0.2839(33)	1.317(41)	−0.433(28)	1.901(57)	−1.167(36)
0.2153(35)	1.395(62)	−0.447(47)	2.009(87)	−1.228(56)
0.1384(43)	1.517(79)	−0.456(60)	2.17(11)	−1.315(71)
0.0939(44)	1.54(11)	−0.521(87)	2.22(15)	−1.372(92)

TABLE XVII. Σ magnetic moments and their quark-sector contributions. Sector contributions are indicated for single quarks having unit charge. Baryon charge states are also summarized. Values for m_π^2 and magnetic moments are in units of GeV^2 and μ_N respectively.

m_π^2	u_{Σ^+}	s_Σ	Σ^+	Σ^0	Σ^-
0.9972(55)	0.976(15)	−0.416(13)	1.440(21)	0.464(7)	−0.512(10)
0.8947(54)	1.010(18)	−0.414(14)	1.484(24)	0.474(8)	−0.535(12)
0.7931(53)	1.044(21)	−0.412(15)	1.530(28)	0.485(9)	−0.559(14)
0.6910(35)	1.072(15)	−0.408(12)	1.565(21)	0.493(7)	−0.579(11)
0.5925(33)	1.113(18)	−0.407(14)	1.620(26)	0.507(8)	−0.607(13)
0.4854(31)	1.163(24)	−0.406(16)	1.686(33)	0.523(10)	−0.640(16)
0.3795(31)	1.221(27)	−0.409(18)	1.764(38)	0.543(12)	−0.678(18)
0.2839(33)	1.286(34)	−0.412(21)	1.852(47)	0.566(14)	−0.720(22)
0.2153(35)	1.344(42)	−0.421(27)	1.932(58)	0.588(18)	−0.756(28)
0.1384(43)	1.418(50)	−0.421(34)	2.031(72)	0.613(23)	−0.805(32)
0.0939(44)	1.446(77)	−0.429(42)	2.07(11)	0.625(30)	−0.821(53)

TABLE XVIII. The Λ^0 magnetic moment and its quark-sector contributions. Sector contributions are indicated for single quarks having unit charge. Baryon charge states are also summarized. Values for m_π^2 and magnetic moments are in units of GeV^2 and μ_N respectively.

m_π^2	u_Λ	s_Λ	Λ^0
0.9972(55)	0.086(10)	1.611(29)	−0.509(9)
0.8947(54)	0.091(12)	1.621(20)	−0.510(10)
0.7931(53)	0.095(13)	1.631(32)	−0.512(10)
0.6910(35)	0.102(11)	1.650(21)	−0.516(8)
0.5925(33)	0.109(12)	1.666(24)	−0.519(8)
0.4854(31)	0.117(14)	1.688(28)	−0.524(10)
0.3795(31)	0.124(16)	1.715(32)	−0.530(11)
0.2839(33)	0.135(18)	1.749(37)	−0.538(13)
0.2153(35)	0.140(24)	1.780(43)	−0.547(16)
0.1384(43)	0.151(27)	1.799(49)	−0.549(18)
0.0939(44)	0.154(31)	1.804(53)	−0.550(20)

well by a dipole. Phenomenologically this is a well established fact for the nucleon at low momentum transfers.

However, we will take an even weaker approximation and assume only that the Q^2 dependence of the electric and magnetic form factors is similar, without stating an explicit functional form for the Q^2 dependence. This too is supported by experiment where the proton ratio $\frac{\mathcal{G}_M(Q^2)}{\mu\mathcal{G}_E(Q^2)} \simeq 1$ for values of Q^2 similar to that probed here. In this case

$$\mathcal{G}_M(0) = \frac{\mathcal{G}_M(Q^2)}{\mathcal{G}_E(Q^2)}\mathcal{G}_E(0). \qquad (5.8)$$

The strange and light sectors of hyperons will scale differently, and therefore we apply Eq. (5.8) to the individual quark sectors. Octet-baryon properties are then reconstructed as described in the discussion surrounding Eq. (4.1) in Sec. IV B. Results for baryon magnetic mo-

ments and their quark-sector contributions are summarized in Tables XVI, XVII, XVIII, and XIX.

1. Quenched chiral perturbation theory

As for the charge radii, it is interesting to compare our results with the LNA and NLNA terms of χPT which survive to some extent in QχPT. As for the charge radii, the NLNA contributions provide little curvature [39] and we turn our attention to the LNA contributions [15]. These LNA contributions to baryon magnetic moments have their origin in couplings of the electromagnetic current to the virtual meson propagating in the intermediate meson-baryon state.

For virtual pion transitions, the LNA terms have the very simple form $\chi m_\pi \sim m_q^{1/2}$, with values for χ as summarized in Tables XIV and XV. While this contribution is finite in the chiral limit, the rate of change of this contribution does indeed diverge in the chiral limit. The less singular nature of this contribution should allow its contributions to be observed at larger pion masses, making magnetic moments an excellent observable to consider in searching for evidence of chiral curvature. Kaon contributions take on the same form in the limit in which baryon mass splittings are neglected.

As for the charge radii, negative values of χ provide curvature towards more positive values as the chiral limit is approached, and vice versa for positive values of χ.

As emphasized earlier in our discussion of charge radii, the flavor-singlet η' meson remains degenerate with the pion in the quenched approximation and makes important contributions to quenched chiral nonanalytic behavior. The neutrality of its charge prevents it from contributing to the coefficients of Tables XIV and XV. However, the double hair-pin diagram in which the vector current couples to the virtual baryon intermediary does give rise to a logarithmic divergence in baryon magnetic moments. However the

TABLE XIX. Ξ magnetic moments and their quark-sector contributions. Sector contributions are indicated for single quarks having unit charge. Baryon charge states are also summarized. Values for m_π^2 and magnetic moments are in units of GeV^2 and μ_N respectively.

m_π^2	s_Ξ	u_{Ξ^0}	Ξ^0	Ξ^-
0.9972(55)	1.132(32)	−0.361(13)	−0.996(23)	−0.635(22)
0.8947(54)	1.137(33)	−0.371(14)	−1.005(24)	−0.634(23)
0.7931(53)	1.141(34)	−0.381(15)	−1.015(24)	−0.634(24)
0.6910(35)	1.152(21)	−0.385(13)	−1.025(18)	−0.640(14)
0.5925(33)	1.157(22)	−0.395(14)	−1.035(19)	−0.640(15)
0.4854(31)	1.163(24)	−0.406(16)	−1.046(20)	−0.640(16)
0.3795(31)	1.172(24)	−0.421(18)	−1.062(21)	−0.641(17)
0.2839(33)	1.181(25)	−0.437(20)	−1.079(23)	−0.642(17)
0.2153(35)	1.189(27)	−0.454(23)	−1.096(25)	−0.642(18)
0.1384(43)	1.199(29)	−0.475(27)	−1.116(29)	−0.641(20)
0.0939(44)	1.212(29)	−0.495(31)	−1.138(32)	−0.643(20)

relatively small couplings of the η' render these contributions negligible at the quark masses probed here [39].

2. Quark-sector magnetic moments

The u-quark contribution to the proton and Σ^+ magnetic moments are illustrated in Fig. 21. The contribution u_p was described as the most optimal channel for directly observing chiral nonanalytic curvature in quenched lattice QCD simulations [15] and this curvature is evident in Fig. 21.

The value of χ for u_p is large and negative, predicting LNA curvature towards positive values as the chiral limit is approached. The value of χ for u_{Σ^+} vanishes in the π channel. Similarly, strength in the ΞK channel is energetically suppressed. Hence the chiral curvature is predicted to be negligible for u_{Σ^+} and will contrast the upward curvature for u_p. This is observed in our lattice simulations. Figure 21 reveals curvature in u_p relative to a rather linear approach for u_{Σ^+} to the chiral limit.

The results for u_p and u_{Σ^+} are highly correlated and therefore the enhancement of the magnetic moment of u in the proton over the Σ^+ provides significant evidence of chiral nonanalytic behavior in accord with the LNA predictions of chiral perturbation theory. The strong correlation of these results is evident in the SU(3) flavor-symmetric point at $m_\pi^2 \simeq 0.5$ GeV^2 where the results are identical. To expose the significance of this result, we present Fig. 22 illustrating the correlated difference of magnetic moment contributions $u_p - u_{\Sigma^+}$. There, the significance exceeds 2 standard deviations for quark masses between the lightest quark mass considered and the SU(3) flavor limit at $m_\pi^2 \simeq 0.5$ GeV^2.

Figure 23 illustrates the magnetic moment contribution of the single u quark in the neutron and the Ξ^0, normalized to unit charge. The magnetic moments match at the SU(3)-flavor limit where $m_\pi^2 \simeq 0.5$ GeV^2 as required. The envi-

FIG. 22 (color online). Correlated difference of u-quark contributions to the magnetic moments of the proton and Σ^+. Chiral curvature in the u-quark contribution to the proton's moment gives rise to significant enhancement in u_p.

ronment sensitivity of the u quark contribution is subtle and is most evident in the size of the statistical error bar.

The chiral coefficient, χ, of the nonanalytic term $\sim m_\pi$ for u_n is large and greater than zero, predicting curvature towards negative values as the chiral limit is approached. While the coefficient for u_{Ξ^0} vanishes in the π channel, a substantial coefficient resides in the energetically favored ΣK channel and therefore some curvature towards negative values might be visible as the chiral limit is approached.

We note that for this case of magnetic moments, there is some evidence of the anticipated chiral curvature. This contrasts the case of charge distribution radii, where chiral curvature was to oppose the Compton-broadening of the distribution and was not manifest in the simulation results.
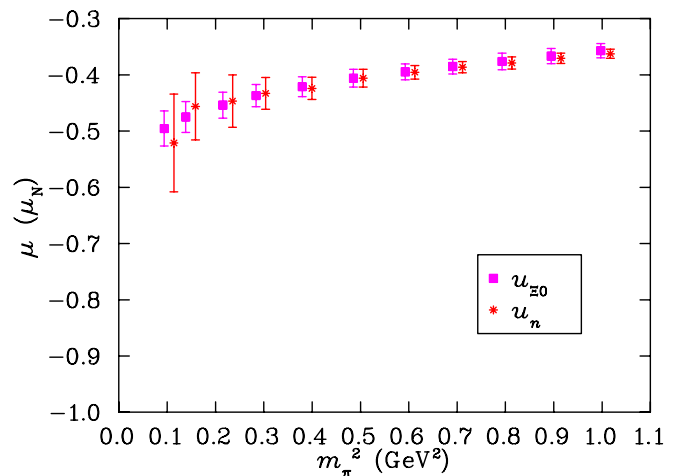

FIG. 21 (color online). Magnetic moment contributions of the u-quark sector to the proton, u_p, and the Σ^+, u_{Σ^+}. The contributions u_p are shifted right for clarity.

FIG. 23 (color online). The u-quark contribution (single quark of unit charge) to the magnetic moments of the neutron, u_n, and Ξ^0, u_{Ξ^0}. The magnetic moment for u_n is shifted to the right for clarity.
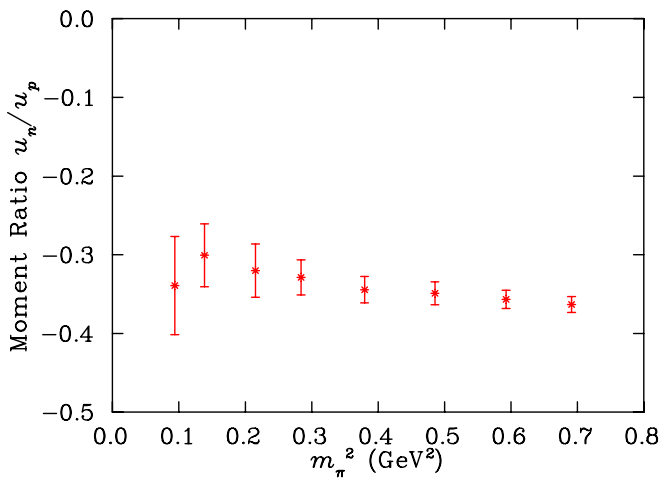
It is interesting to examine the ratio of singly (u_n) and doubly (u_p) represented quark contributions (for single quarks of unit charge) to nucleon magnetic moments [4]. The SU(6) spin-flavor symmetry of the simple quark model provides

$$\mu_p = \tfrac{4}{3}\mu_u - \tfrac{1}{3}\mu_d, \tag{5.9}$$

$$= \tfrac{2}{3}2\tfrac{2}{3}\mu_q^{\text{QM}} - \tfrac{1}{3}1(-\tfrac{1}{3})\mu_q^{\text{QM}}, \tag{5.10}$$

where μ_q^{QM} is the constituent quark moment. The quark moment prefactors in Eq. (5.10) are, respectively, SU(6), quark number and charge factors. Discarding quark number and charge factors, one arrives at the SU(6) prediction for u_n/u_p for single quarks of unit charge of $-1/2$. This prediction is to be compared with Fig. 24 which reveals this ratio to be substantially smaller than the SU(6) prediction, even at the SU(3) flavor-symmetric limit where $m_\pi^2 \simeq 0.5$ GeV^2. This result is in accord with Ref. [4] where this effect was first observed in lattice QCD.

The gentle slope of the results in Fig. 24 at larger quark masses suggests that the SU(6) spin-flavor-symmetric quark model prediction of $-1/2$ will be realized only at much heavier quark masses than those examined here.

Figure 25 shows the magnetic moment contribution of the u-quark sector (or equivalently the d-quark sector) to the Λ^0 magnetic moment, normalized for a single quark of unit charge. In simple quark models, this contribution is zero as the u and d quarks are in a spin-0, isospin-0 state. Our simulation results reveal that the dynamics of QCD, even in the quenched approximation, are much more complex. The contribution of u_Λ differs from zero by more than 8 standard deviations at the SU(3) flavor-symmetric point, and confirms earlier findings [4] of a nontrivial role for the light quark sector in the magnetic moment of Λ^0.

FIG. 25.   Magnetic moment contribution of the u-quark sector (or equivalently the d-quark sector) to the Λ^0 magnetic moment.

The chiral coefficient for u_Λ vanishes in the pion channel and has only small strength in the energetically favored NK channel. Hence little curvature is anticipated and this is supported by our findings in Fig. 25.

Turning our attention to the strange-quark sectors, Figs. 26 and 27 present results for s_Λ, s_Ξ, and s_Σ magnetic moments. In our simulations the strange-quark mass is held fixed and therefore any variation observed in the results is purely environmental in origin. While s_Ξ and s_Σ display only a mild environment sensitivity, s_Λ shows a remarkably-robust dependence on its light-quark environment.

Recall that in our examination of the environmental flavor-symmetry dependence of the strange-quark distribution, a strong sensitivity was found. When the environmental quarks are in an isospin-0 state in the Λ, the strange-quark distribution is broad. On the other hand, when the

FIG. 24 (color online).   The ratio of singly (u_n) and doubly (u_p) represented quark contributions for single quarks of unit charge to nucleon magnetic moments. In the simple SU(6) spin-flavor-symmetric quark model the predicted ratio is constant at $-1/2$.
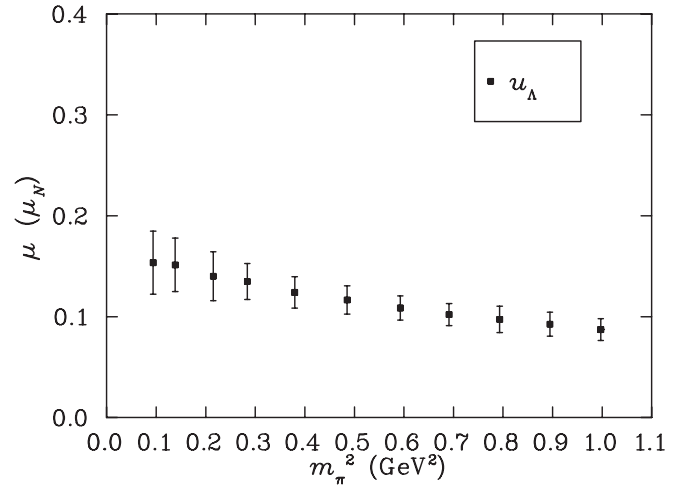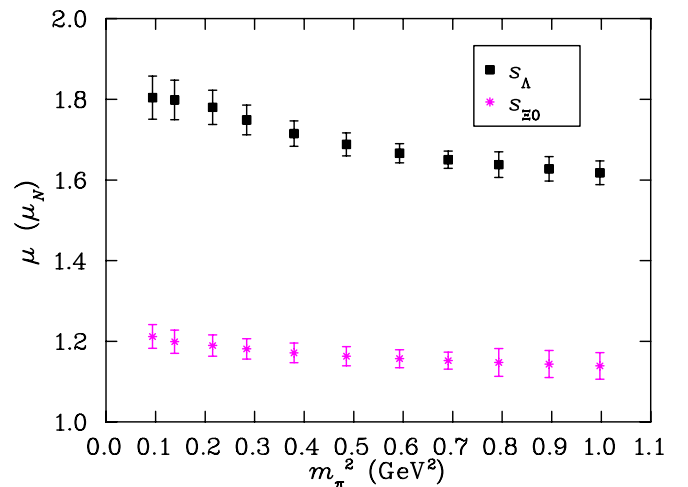

FIG. 26 (color online).   Magnetic moments of s_Λ and s_{Ξ^0} as a function of quark mass.
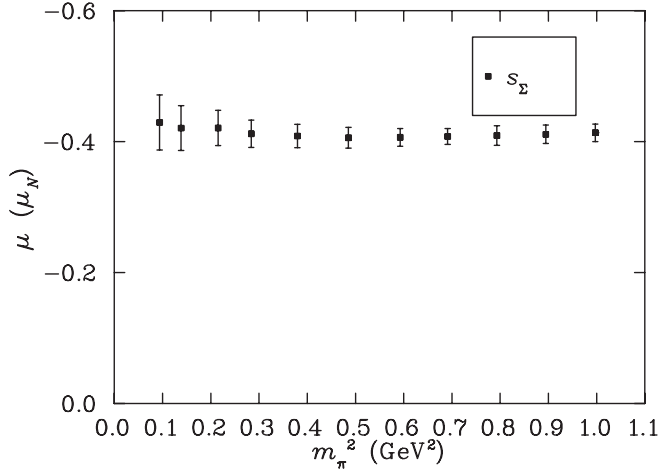
FIG. 27. Magnetic moment contribution of the strange quark in Σ, s_Σ, as a function of quark mass.

FIG. 28 (color online). Magnetic moments of Σ^-, Λ^0, and Ξ^-. Results for Λ^0 and Ξ^- are offset left and right, respectively, for clarity.

environmental quarks are in an isospin-1 state in Σ baryons, the distribution radius is significantly smaller. It appears that the broad distribution of the strange quark in Λ makes it sensitive to the dynamics of its neighbors.

In the case of strange-quark moments, the LNA contributions are exclusively from transitions involving the kaon. Referring to Table XIV, one sees that both s_Λ and s_Ξ have strong transitions to the energetically favorable KN and $K\Sigma$ channels, respectively. The coefficients are negative such that the virtual transitions will act to provide subtle curvature towards positive values, enhancing the magnetic moments in these cases. This is not the case for s_Σ where the sign is positive and the transition is to the energetically unfavored $K\Xi$ channel. In summary, QχPT suggests the magnetic moments for s_Λ and s_Ξ will display subtle curvature that acts to enhance the magnetic moment whereas s_Σ will display little curvature.

3. Baryon magnetic moments

Figure 28 depicts the magnetic moments of Λ^0, Σ^-, and Ξ^-. As the magnetic moments of Λ^0 and Ξ^- are dominated by the strange-quark contribution, these moments show only a gentle dependence on the quark mass. These contrast Σ^- where the light d quarks dominate the moment. However, the curvature in the Λ^0 moment towards negative values contrasts the invariance of the Ξ^-.

The hyperon charge states, Σ^- and Ξ^-, have LNA chiral coefficients which vanish in quenched QCD. On the other hand, the Λ^0 magnetic moment has some positive strength in the energetically favored NK channel, predicting subtle curvature towards negative values as the chiral limit is approached.

Figure 29 presents results for the Σ^0 baryon where chiral curvature is anticipated to be small. However, a comparison of p and Σ^+ magnetic moments provides a favorable opportunity to observe chiral curvature. The proton has a strong negative coupling to the pion channel, predicting
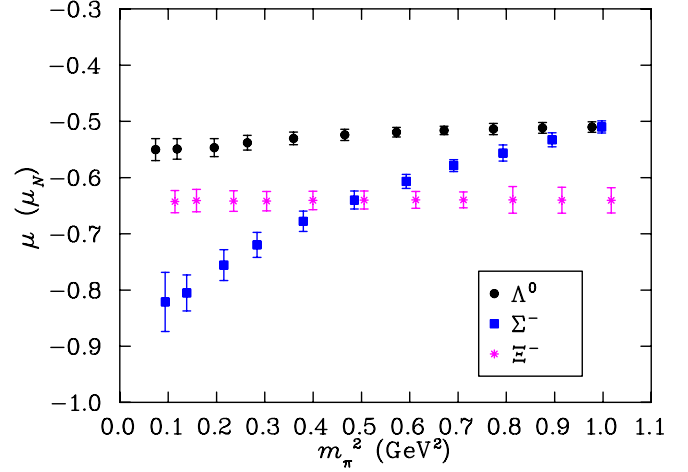
curvature towards positive values as the chiral limit is approached. This contrasts the Σ^+ where the strong coupling is to the energetically unfavorable ΞK channel suggesting a more linear approach to the chiral limit.

Figure 30 depicts the variation of these moments with quark mass. The strong correlation of these results is evident in the SU(3) flavor-symmetric point at $m_\pi^2 \simeq 0.5$ GeV^2 where the results are identical. The enhancement of the magnetic moment of the proton over the Σ^+ is best illustrated in Fig. 31 where the correlated differences in the baryon moments are plotted as a function of m_π^2. This provides significant evidence of curvature in accord with the LNA predictions of chiral perturbation theory.

Figure 32 reports the magnetic moments of the neutron and Ξ^0. The neutron provides a favorable case for the observation of chiral curvature associated with the pion channel. Similarly the Ξ^0 has significant strength in the energetically favored ΣK channel. In both cases the chiral
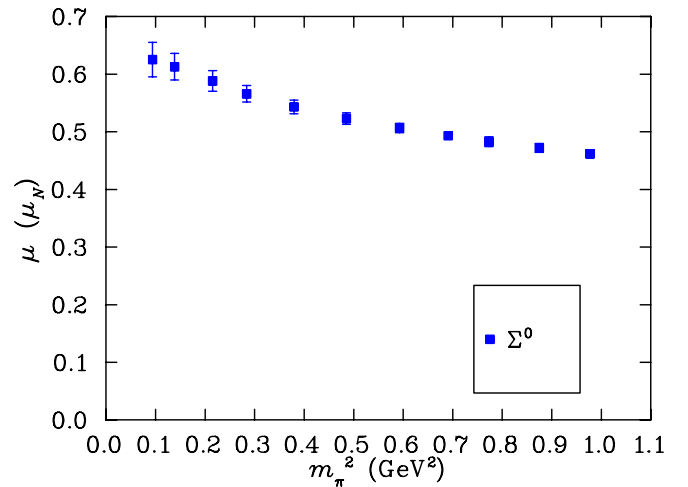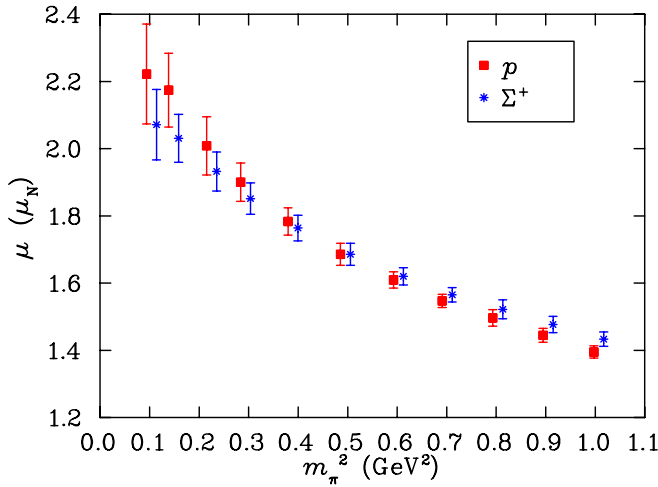

FIG. 29 (color online). Magnetic moment of Σ^0.

FIG. 30 (color online). Magnetic moments of the proton and Σ^+. The Σ^+ moments are offset to the right for clarity.

coefficient, χ is positive, predicting curvature towards negative values as the chiral limit is approached.

In summary, we have performed an unprecedented exploration of the light-quark-mass properties of octet-baryon magnetic moments in quenched QCD. Figure 33 presents our results in the context of recent state of the art results from lattice QCD using similar three-point function techniques [4,5,12]. The precision afforded by 400, $20^3 \times 40$ lattices and the efficient access to the chiral regime enabled by our use of the FLIC fermion action is clear.

4. Ratio of μ_{Ξ^-} to μ_Λ

The experimentally measured value of magnetic moment of Ξ^- is -0.651 ± 0.003 μ_N and that of Λ is -0.613 ± 0.004 μ_N, making their ratio greater than 1 at 1.062 ± 0.012. This has presented a long-standing problem to constituent quark models which predict the magnetic moment ratio, Ξ^-/Λ^0, to be less than one.
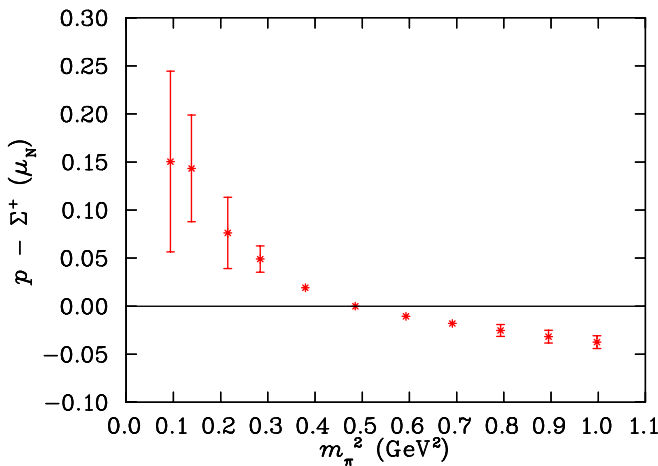
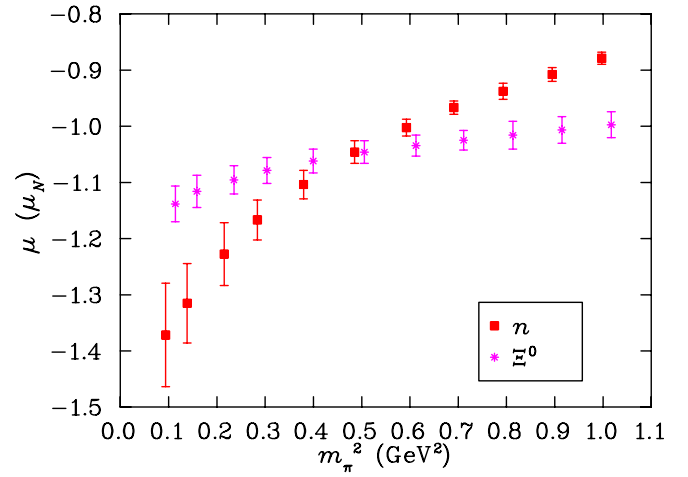FIG. 31 (color online). Correlated difference in the magnetic moments of the proton and Σ^+.

FIG. 32 (color online). Magnetic moments of the neutron and Ξ^0. Ξ^0 moments are offset to the right for clarity.

In the simple SU(6) spin-flavor quark model, the magnetic moment of Ξ^- is

$$\mu_{\Xi^-} = \tfrac{4}{3}\mu_s - \tfrac{1}{3}\mu_d, \tag{5.11}$$

where μ_s and μ_d are the magnetic moments of the constituent s and d quarks, respectively. Since the u-d pair in Λ forms a spin-0 state, the magnetic moment of the Λ has a sole contribution from the s quark

$$\mu_\Lambda = \mu_s. \tag{5.12}$$
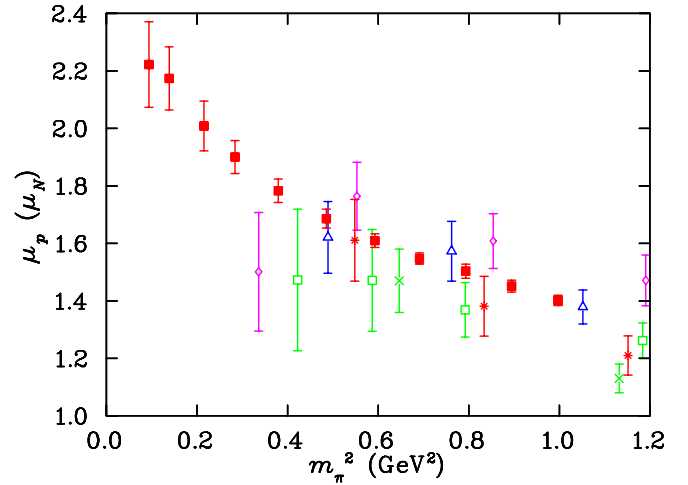
Taking the ratio yields

FIG. 33 (color online). The proton magnetic moment in nuclear magnetons is compared with a variety of lattice simulations using three-point function techniques. The solid squares indicate our current lattice QCD results with FLIC fermions. The stars indicate the early lattice results of Ref. [4]. The crosses (only one point) indicate the results of Ref. [5]. The open symbols describe the QCDSF Collaboration results [12]. Open squares indicate results with $\beta = 6.0$, open triangles indicate those with $\beta = 6.2$ while the open diamonds indicate their results with $\beta = 6.4$.
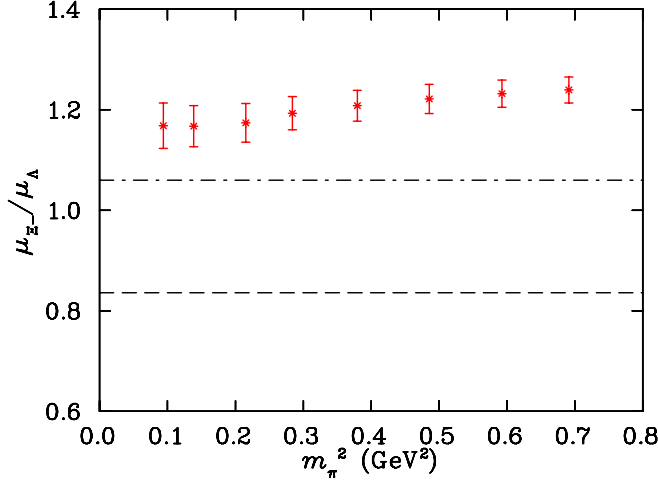
FIG. 34 (color online). Magnetic moment ratio μ_{Ξ^-}/μ_Λ as calculated in quenched QCD. The simple quark model results of 0.836 is illustrated by the dashed line while the experimental value of the ratio is indicated by the dashed-dotted line.

$$\frac{\mu_{\Xi^-}}{\mu_\Lambda} = \frac{4}{3} - \frac{1}{3}\frac{\mu_d}{\mu_s}. \qquad (5.13)$$

Now since, the magnetic moment of a charged Dirac particle goes inversely as its mass, and since the s and d quarks have identical charge, the ratio may be written

$$\frac{\mu_{\Xi^-}}{\mu_\Lambda} = \frac{4}{3} - \frac{1}{3}\frac{m_s}{m_d}, \qquad (5.14)$$

where m_d and m_s are the constituent masses of the d and s quarks, respectively. Given that $m_s > m_d$ it is inescapable that this ratio is less than 1 in the simple quark model. Indeed, the accepted values of d and s constituent quark masses place this ratio at 0.836.

Figure 34 shows the μ_{Ξ^-}/μ_Λ ratio as a function of quark mass as observed in our quenched lattice calculations. Remarkably, the ratio is greater than one at all quark masses.

There are two important aspects of our previous discussion that give rise to a result exceeding 1. First, as illustrated in Fig. 24, we have found that the singly-represented quarks give a contribution to the magnetic moment that is much smaller in magnitude than that of the SU(6) quark model prediction. This gives rise to a 40% reduction in the contribution of the second term of Eq. (5.14).

While this is sufficient to correct the ratio to ~ 1, there is a second effect. Namely, the light quark sector makes a nontrivial contribution to the Λ magnetic moment. As illustrated in Fig. 25, this contribution is positive for unit charge quarks. Since the net charge of the u-d sector is $+1/3$, the contribution of the s quark in Λ^0 must have a negative value whose magnitude exceeds the observed Λ moment. And this is seen in Fig. 26. There, chiral curvature in s_Λ makes the ratio of magnetic moment contributions $s_\Lambda/s_\Xi \sim 3/2$ as opposed to the SU(6) suggestion of 4/3. This resolves the long-standing discrepancy.

C. Magnetic radii

Using the values for the magnetic moments obtained by scaling the individual quark-sector contributions to $Q^2 = 0$, and our values for the form factors at finite Q^2, magnetic radii may be determined in exactly the same fashion as the electric radii.

Analogous to the charge radius, we adopt a dipole form for the Q^2 dependence and define the magnetic radius as

$$\frac{\langle r_M^2 \rangle}{G_M(0)} = \frac{12}{Q^2}\left(\sqrt{\frac{G_M(0)}{G_M(Q^2)}} - 1\right). \qquad (5.15)$$

The magnetic radii, $\langle r_M^2 \rangle / G_M(0)$, are tabulated in Table XX. Figs. 35 through 38 display the variation of the magnetic radii with m_π^2 for the octet baryons.

Figure 35 depicts the magnetic radii of the proton and Σ^+ as a function of input quark mass. The somewhat subtle differences have a simple explanation in terms of the more localized strange quark in Σ.

In the proton, the long-range nature of the light-quark distributions means that their contributions to the magnetic

TABLE XX. Magnetic radii $\langle r_M^2 \rangle / G_M(0)$ of the octet baryons in fm^2 for various m_π^2 in GeV^2.

m_π^2	p	n	Σ^+	Σ^0	Σ^-	Λ	Ξ^0	Ξ^-
0.9972(55)	0.241(7)	0.240(6)	0.254(9)	0.264(9)	0.236(10)	0.328(14)	0.298(13)	0.337(16)
0.8947(54)	0.255(8)	0.252(7)	0.265(10)	0.273(9)	0.252(10)	0.328(14)	0.302(13)	0.335(17)
0.7931(53)	0.269(9)	0.266(9)	0.278(10)	0.283(10)	0.269(12)	0.328(16)	0.306(13)	0.334(17)
0.6910(35)	0.286(9)	0.283(8)	0.292(10)	0.294(9)	0.287(11)	0.339(14)	0.314(12)	0.340(14)
0.5925(33)	0.305(10)	0.301(10)	0.308(11)	0.308(11)	0.309(12)	0.340(15)	0.319(12)	0.339(15)
0.4854(31)	0.330(14)	0.326(13)	0.330(14)	0.326(13)	0.337(15)	0.342(17)	0.326(13)	0.337(15)
0.3795(31)	0.356(17)	0.351(16)	0.352(16)	0.344(15)	0.365(18)	0.343(18)	0.334(14)	0.334(16)
0.2839(33)	0.387(21)	0.382(21)	0.377(19)	0.364(18)	0.396(22)	0.348(20)	0.343(16)	0.332(16)
0.2153(35)	0.415(27)	0.413(28)	0.395(24)	0.380(22)	0.418(27)	0.353(22)	0.352(17)	0.330(16)
0.1384(43)	0.438(31)	0.439(32)	0.428(32)	0.407(29)	0.462(36)	0.351(22)	0.365(19)	0.328(17)
0.0939(44)	0.470(48)	0.478(50)	0.446(42)	0.423(38)	0.483(49)	0.347(24)	0.384(22)	0.336(18)
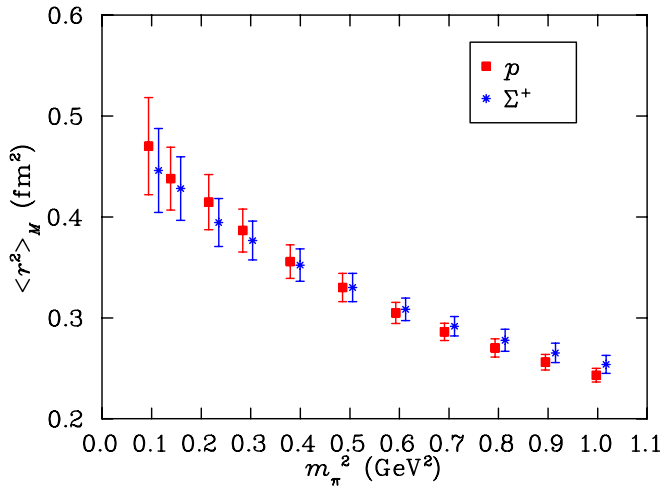
FIG. 35 (color online). Magnetic radii of the proton and Σ^+. The latter are shifted right for clarity.

FIG. 37 (color online). Magnetic radii of Σ^0 and Λ. The latter are shifted left for clarity.

form factor reduce quickly for increasing momentum transfers. In the case of Σ^+, which has a broadly distributed u quark distribution and a narrowly distributed s quark distribution, the reduction in magnitude of the form factor is less. Here, the s-quark distribution contributes positively and remains relatively invariant with increased resolution. Thus the Σ^+ has a larger form factor than the proton at finite Q^2 and hence a smaller magnetic radius.

Figure 36 reports the magnetic radii of the neutron and Ξ^0. Following a similar argument as above, the neutron is expected to have a larger magnetic radius than the Ξ^0, and this is confirmed in the plot.

Figure 37 illustrates the magnetic radii of Λ and Σ^0 as a function of the input quark mass. In Λ, most of the magnetic moment has its origin in the s quark and therefore the magnetic radius will be relatively small. In the Σ^0 the u-d sector is a major contributor to the form factor. As a result,

the form factor reduces more at finite momentum transfer, which in turn implies that the magnetic radius of the Σ^0 will be relatively large.

Figure 38 illustrates the magnetic radii of Σ^-, Σ^+ and Ξ^-. Σ^+ is replotted here to facilitate comparison with the other two members of the baryon octet.

Σ^- has the largest magnetic radius among the octet baryons and this is to be expected based on our considerations of the origin of the baryon magnetic moment. Here, the doubly-represented d quark contributes to the total baryon form factor with the same sign, whereas the strange sector acts to reduce the magnitude of the total form factor. Upon increasing the momentum transfer resolution, the d-sector is reduced dramatically whereas the strange sector, acting to reduce the total form factor, is relatively
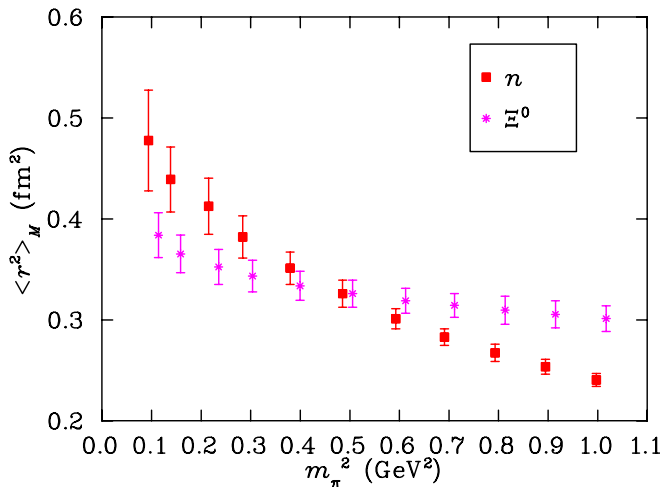

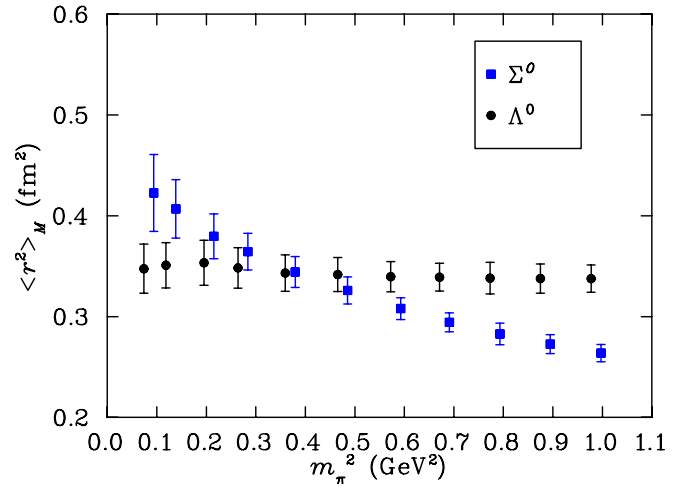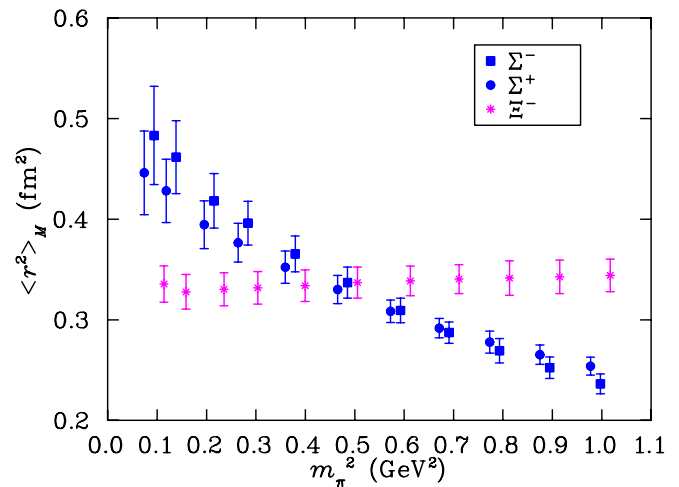FIG. 36 (color online). Magnetic radii of the neutron and Ξ^0. The latter are shifted to the right for clarity.

FIG. 38 (color online). Magnetic radii of Σ^+, Σ^-, and Ξ^-. Results for Σ^+ and Ξ^- are offset left and right, respectively, for clarity.

preserved. this gives rise to a large drop in the total form factor at finite Q^2 and thus a large magnetic radius.

On the other hand, the singly-represented d quark in the Ξ^- makes only a small contribution to the Ξ^- form factor, and therefore the magnetic radius reflects the small distribution of the strange quark.

VI. SUMMARY

We have presented an extensive investigation of the electromagnetic properties of octet baryons in quenched QCD. The development of the $\mathcal{O}(a)$-improved FLIC fermion action has been central to enabling this study. The FLIC fermion operator is an efficient nearest-neighbor fermion operator with excellent scaling properties [28]. The vastly improved chiral properties of this operator [29] enables the exploration of the electromagnetic form factors at quark masses significantly lighter than those investigated in the past. The unprecedented nature of our quark masses is illustrated in Figs. 20 and 33 for the proton charge radii and magnetic moments, respectively.

Central to our discussion of the results is the search for evidence of chiral nonanalytic behavior as predicted by chiral perturbation theory. We have discovered that all baryons having nonvanishing, energetically- favorable couplings to virtual meson-baryon transitions tend to be broader than those which do not. This qualitative realization provides a simple explanation for the patterns revealed in our quenched-QCD simulations.

Of particular interest is the environmental isospin dependence of the strange-quark distributions in Λ^0 and Σ^0. When the environmental quarks are in an isospin-0 state in the Λ, the strange-quark distribution is broad. On the other hand, when the environmental quarks are in an isospin-1 state in Σ baryons, the distribution radius is significantly smaller.

Still, evidence of chiral *curvature* on our large-volume lattice is rather subtle in general and absent in the exceptional case of the singly-represented quark in the neutron or Ξ. In this case, the chiral-loop effects act to oppose the Compton broadening of the distribution. However, it is thought that the restriction of momenta to discrete values on the finite-volume lattice prevents the build up of strength in the loop integral sufficient to counter the natural broadening of the distribution as the quark becomes light. It will be interesting to explore this quantitatively in finite-volume chiral effective field theory.

In contrast, chiral curvature is evident in the quark-sector contributions to baryon magnetic moments. In every case, the curvature predicted by chiral perturbation theory is in accord with our results. Of particular mention is the comparison of the u-quark contribution to the proton and Σ^+ illustrated in Figs. 21 and 22. The environment sensi-

tivity of the s quark in Λ^0 depicted in Fig. 26 is particularly robust.

We find it remarkable that the features predicted by the coefficients of the leading nonanalytic terms of quenched chiral perturbation theory are observed in our simulation results. Naively, one might have expected a different role for the higher order terms of the chiral expansion which might have acted to hide the leading behavior. However, the smooth and slow variation of our simulation results indicate the presence of correlations between the coefficients of nonanalytic terms in general. Obviously the chiral expansion must sum to provide only a small correction to the almost linear behavior observed away from the chiral limit. These observations indicate that regularizations of chiral effective field theory which resum the chiral expansion at each order, to ensure that higher order terms sum to only small corrections, will be effective in performing quantitative extrapolations to the physical point. Indeed work in this direction [9,11,39] has been very successful.

Comparison of our quenched-QCD results with experiment is not as interesting. The chiral physics of quenched QCD differs from the correct chiral physics of full QCD and our results explore sufficiently light-quark masses to reveal these discrepancies. The simulation results do not agree with experiment, particularly for light-quark baryons where chiral physics makes significant contributions. However, methods have been discovered for quantitatively estimating the corrections to be encountered in simulating full QCD and we refer the interested reader to Refs. [9,11,39] for further discussion.

In future simulations it will be interesting to explore the utility of boundary conditions which allow access to arbitrarily small momentum transfers, providing opportunities to map out hadron form factors in detail. Similarly, by calculating near $Q^2 = 0$ one would have more direct access to the magnetic moment. Nevertheless, such boundary conditions cannot be seen to substitute for larger volume lattices, as the discretization of the momenta due to the finite volume of the lattice acts to suppress chiral nonanalytic behavior. Only with increasing lattice volumes will the continuous momentum of chiral loops be approximated well on the lattice.

[1] W. Wilcox and R. M. Woloshyn, Phys. Rev. Lett. **54**, 2653 (1985); R. M. Woloshyn and A. M. Kobos, Phys. Rev. D **33**, 222 (1986); R. M. Woloshyn, Phys. Rev. D **34**, 605 (1986); T. Draper, R. M. Woloshyn, W. Wilcox, and K. F. Liu, Nucl. Phys. **B318**, 319 (1989).

[2] G. Martinelli and C. T. Sachrajda, Nucl. Phys. **B306**, 865 (1988); **B316**, 355 (1989).

[3] T. Draper, R. M. Woloshyn, and K. F. Liu, Phys. Lett. B **234**, 121 (1990).

[4] D. B. Leinweber, R. M. Woloshyn, and T. Draper, Phys. Rev. D **43**, 1659 (1991).

[5] W. Wilcox, T. Draper, and K. F. Liu, Phys. Rev. D **46**, 1109 (1992).

[6] D. B. Leinweber, T. Draper, and R. M. Woloshyn, Phys. Rev. D **46**, 3067 (1992).

[7] D. B. Leinweber, T. Draper, and R. M. Woloshyn, Phys. Rev. D **48**, 2230 (1993).

[8] J. M. Zanotti, S. Boinepalli, D. B. Leinweber, A. G. Williams, and J. B. Zhang, Nucl. Phys. B, Proc. Suppl. **128**, 233 (2004).

[9] D. B. Leinweber *et al.*, Phys. Rev. Lett. **94**, 212001 (2005).

[10] D. B. Leinweber *et al.*, Eur. Phys. J. A **24S2**, 79 (2005).

[11] D. B. Leinweber *et al.*, Phys. Rev. Lett. **97**, 022001 (2006).

[12] M. Gockeler *et al.* (QCDSF Collaboration), Phys. Rev. D **71**, 034508 (2005).

[13] R. G. Edwards *et al.* (LHPC Collaboration), Proc. Sci., LAT2005 (2005) 056.

[14] F. X. Lee, R. Kelly, L. Zhou, and W. Wilcox, Phys. Lett. B **627**, 71 (2005).

[15] D. B. Leinweber, Phys. Rev. D **69**, 014005 (2004).

[16] M. J. Savage, Nucl. Phys. **A700**, 359 (2002).

[17] N. Mathur and S. J. Dong, Nucl. Phys. B, Proc. Suppl. **94**, 311 (2001); S. J. Dong *et al.*, Phys. Rev. D **58**, 074504 (1998).

[18] R. Lewis, W. Wilcox, and R. M. Woloshyn, Phys. Rev. D **67**, 013003 (2003).

[19] J. Foley, K. Jimmy Juge, A. O'Cais, M. Peardon, S. M. Ryan, and J. I. Skullerud, Comput. Phys. Commun. **172**, 145 (2005).

[20] D. B. Leinweber, Phys. Rev. D **45**, 252 (1992).

[21] D. B. Leinweber, Phys. Rev. D **47**, 5096 (1993).

[22] D. B. Leinweber and A. W. Thomas, Phys. Rev. D **62**, 074505 (2000).

[23] M. Luscher and P. Weisz, Commun. Math. Phys. **97**, 59 (1985); **98**, 433 (1985).

[24] R. Sommer, Nucl. Phys. **B411**, 839 (1994).

[25] J. M. Zanotti *et al.*, Phys. Rev. D **65**, 074507 (2002); Nucl. Phys. B, Proc. Suppl. **109**, 101 (2002).

[26] S. O. Bilson-Thompson *et al.*, Ann. Phys. (N.Y.) **304**, 1 (2003).

[27] J. J. Sakurai, *Advanced Quantum Mechanics* (Addison-Wesley, Reading, MA, 1982).

[28] J. M. Zanotti, B. Lasscock, D. B. Leinweber, and A. G. Williams, Phys. Rev. D **71**, 034510 (2005).

[29] S. Boinepalli, W. Kamleh, D. B. Leinweber, A. G. Williams, and J. M. Zanotti, Phys. Lett. B **616**, 196 (2005).

[30] S. Gusken, Nucl. Phys. B, Proc. Suppl. **17**, 361 (1990).

[31] J. M. Zanotti *et al.*, Phys. Rev. D **68**, 054506 (2003).

[32] G. Martinelli, C. T. Sachrajda, and A. Vladikas, Nucl. Phys. **B358**, 212 (1991).

[33] T. Draper, R. M. Woloshyn, W. Wilcox, and K. F. Liu, Nucl. Phys. B, Proc. Suppl. **9**, 175 (1989).

[34] W. Melnitchouk *et al.*, Phys. Rev. D **67**, 114506 (2003).

[35] D. B. Leinweber, W. Melnitchouk, D. G. Richards, A. G. Williams, and J. M. Zanotti, Lect. Notes Phys. **663**, 71 (2005).

[36] D. B. Leinweber and T. D. Cohen, Phys. Rev. D **47**, 2147 (1993).

[37] D. Arndt and B. C. Tiburzi, Phys. Rev. D **68**, 094501 (2003).

[38] S. Boinepalli *et al.* (CSSM Lattice Collaboration) (unpublished).

[39] R. D. Young, D. B. Leinweber, and A. W. Thomas, Phys. Rev. D **71**, 014001 (2005).